Eur. Phys. J. C (2025) 85:1340
https://doi.org/10.1140/epjc/s10052-025-15000-4

THE EUROPEAN PHYSICAL JOURNAL C

Regular Article - Theoretical Physics

Gravitational wave radiation from periodic orbits and quasi-periodic oscillations in an Einstein nonlinear Maxwell–Yukawa black hole

Tehreem Zahra[1,a], **Oreeda Shabbir**[1,b], **Bushra Majeed**[2,c], **Mubasher Jamil**[1,3,d], **Javlon Rayimbaev**[4,5,e], **Abubakir Shermatov**[6,7,8,f]

[1] School of Natural Sciences, National University of Sciences and Technology (NUST), Islamabad 44000, Pakistan
[2] College of Electrical and Mechanical Engineering (CEME), National University of Sciences and Technology, Islamabad 44000, Pakistan
[3] Research Center of Astrophysics and Cosmology, Khazar University, 41 Mehseti Street, Baku 1096, Azerbaijan
[4] National University of Uzbekistan, Tashkent 100174, Uzbekistan
[5] Urgench State University, Kh. Alimdjan Str. 14, Urgench 220100, Uzbekistan
[6] Institute of Fundamental and Applied Research, National Research University TIIAME, Kori Niyoziy 39, Tashkent 100000, Uzbekistan
[7] University of Tashkent for Applied Sciences, Str. Gavhar 1, Tashkent 100149, Uzbekistan
[8] Tashkent State Technical University, Tashkent 100095, Uzbekistan

Received: 18 July 2025 / Accepted: 26 October 2025

Abstract In this article, we investigate the orbital dynamics and quasi-periodic oscillations (QPOs) surrounding a static, spherically symmetric geometry of an Einstein–nonlinear Maxwell—Yukawa (ENLMY) black hole (BH). Using the Hamiltonian formalism, we derive equations of motion and analyze the effective potential. We determine the innermost stable circular orbit (ISCO) and innermost bound circular orbit (IBCO) radii for different values of the Yukawa parameters λ and δ, and classify periodic orbits via rational frequency analysis, highlighting deviations from Schwarzschild geometry. We also study gravitational wave (GW) emission from periodic orbits and show how Yukawa terms affect GW signals. Fundamental frequencies are computed, and QPOs are analyzed using relativistic precession, warped disk, and tidal disruption models. By increasing λ, the ENLMY spacetime effectively mimics the behavior of a Schwarzschild spacetime. Constraints on the BH mass and Yukawa parameters are derived using QPO data from stellar-mass (XTE J1550-564, GRO J1655-40, GRS 1915+105), intermediate-mass (M82 X-1), and supermassive (SgrA*) BHs within the relativistic precession model by employing a Markov chain Monte Carlo analysis.

1 Introduction

General Relativity (GR) has been remarkably successful in describing gravitational phenomena, from solar system tests to gravitational wave (GW) detection [1–6]. However, it lacks a consistent quantum description [7] and fails at singularities. Additionally, GR faces challenges in describing the accelerated expansion of the universe without invoking unknown components, such as dark matter (DM) and dark energy (DE). There is no direct evidence for the existence of DM, and a theoretical framework to describe its behavior is still lacking [8,9]. These limitations have motivated the development of modified theories of gravity, which can be done either by introducing new matter fields or by altering the geometric structure of spacetime [10–12]. Among the latter is $f(R)$ gravity, which modifies the Einstein–Hilbert action by promoting the Ricci scalar R to a more general function $f(R)$. Such modifications naturally introduce additional degrees of freedom and can provide alternative explanations for cosmological and galactic dynamics without the need for unknown matter components. In the weak-field limit, $f(R)$-gravity yields Yukawa-like corrections to the gravitational potential. Such a correction carries a characteristic length scale that can effectively screen gravitational modifications at solar

[a] e-mail: tehreemzahra971@gmail.com
[b] e-mail: oreedashabbir7@gmail.com
[c] e-mail: bushra.majeed@ceme.nust.edu.pk
[d] e-mail: mjamil@sns.nust.edu.pk (corresponding author)
[e] e-mail: javlon@astrin.uz
[f] e-mail: shermatov.abubakir98@gmail.com

Published online: 21 November 2025

system scales while revealing deviations in the strong-field regime [13]. Hence, these extended theories must be thoroughly tested in astrophysical environments to determine their validity. In this context, black holes (BHs), as the most compact and extreme gravitational objects in the universe, provide a natural setting for testing gravitational theories in the strong-field regime [14].

The properties of geodesic orbits are deeply connected to the underlying BH geometry. Among these, periodic orbits play a crucial role in understanding orbital dynamics [15], both in astrophysical contexts, such as planetary motion in the Solar System, and in more extreme environments, like galactic centers. In particular, periodic orbits are essential for analyzing the long-term stability of bound systems and offer valuable insights into the evolution of extreme mass-ratio inspirals (EMRIs) [16]. An EMRI system is formed by a stellar-mass object orbiting around a central supermassive BH [17]. During the adiabatic inspiral phase, periodic orbits serve as transitional paths that significantly influence the GWs emitted by such systems [18]. These waveforms are highly sensitive to the orbital configuration, making periodic geodesics vital for GW detection and signal interpretation. These orbits often exhibit zoom-whirl behavior, with the test particle returning to its initial location after a finite time [19]. In [20–22], periodic orbits in Schwarzschild, Kerr, and naked singularity spacetimes are investigated extensively. In this work, we investigate timelike periodic geodesic orbits in the spacetime of a Yukawa-like BH. In addition to identifying such orbits, we examine the parameter space of angular momentum and energy that permits bound motion in this modified gravitational background, thereby understanding how deviations from GR affect orbital structure.

Studying the spectroscopic properties of accretion disks around compact astrophysical objects (neutron stars, BHs, and hypothetical wormholes) through Fourier analysis of their X-ray emissions provides a powerful method for probing spacetime structure and revealing characteristic accretion processes. In X-ray binary systems (XRBs) with BHs or neutron stars and companion stars, the central object's gravity affects radiation processes in the accretion disk [23]. Such analyses have identified quasi-periodic oscillations (QPOs), which are peaks observed in the power density spectrum of X-ray emissions [24]. These are categorized as high-frequency (HF, 50–450 Hz) or low-frequency (LF, 0.01–30 Hz) QPOs [25]. Precise QPO measurements in microquasars and quasars offer insights into spacetime properties near BHs, enabling tests of gravity theories, constraints on BH parameters, and determination of the innermost stable circular orbit (ISCO) radius.

Previous studies [26–34] suggest that QPO orbits may help estimate the ISCO radius within observational uncertainties. Additionally, the capture of massless and massive particles by parameterized BHs has been examined [35–37], while orbital and epicyclic frequencies in axially symmetric spacetimes are explored in [38–40]. Recent numerical studies have investigated QPO generation mechanisms by solving general relativistic hydrodynamic equations [41] in Kerr and hairy metrics. These simulations reveal spiral shock waves formed by plasma perturbations in strong gravitational fields, linking them to QPO formation [42–44]. Similarly, Bondi–Hoyle–Lyttleton accretion models describe shock cone dynamics and their role in producing QPO frequencies [45–47]. Such shocks may explain LF/HF QPOs in sources like GRS 1915+105 [48] and predict QPOs near the M87 BH [49]. However, the physical origin of QPOs is still unknown. Following the initial detection of QPOs, various theoretical models have been proposed to interpret their origin, including disko-seismic oscillations, relativistic precession (RP) model, tidal disruption (TD) model, the warped disk (WD) model, and resonance models [50]. Using the RP model, constraints on the parameters of XRBs have also been found using statistical techniques in literature [51–55]. In the present work, we also calculate oscillation frequencies and apply them to QPOs to obtain constraints on the black hole and Einstein–nonlinear Maxwell—Yukawa (ENLMY) gravity parameters using Markov chain Monte Carlo (MCMC) analyses.

This paper explores the dynamics of test particles around an ENLMY BH, and the analysis will be carried out by studying the periodic orbits and QPOs. We emphasize that the Yukawa corrections are not just mathematical artifacts but physical mechanisms of screening that allow the ENLMY geometry to interpolate between GR and modified gravity regimes. This feature makes ENLMY black holes particularly suitable for testing intermediate-scale deviations from GR in astrophysical environments. The outline of this paper is as follows: In Sect. 2, we introduce the ENLMY metric. In Sect. 3, the dynamics of test particles around an ENLMY BH are studied, including the effective potential and energy efficiency. Section 4 focuses on the effective potential and the conditions for circular orbits, including a detailed analysis of ISCOs and innermost bound circular orbits (IBCOs). Section 5 investigates periodic orbits, analyzing their structure and behavior within the framework of the underlying spacetime geometry. In section 6, we examine the GW radiation emitted by periodic orbits in the ENLMY BH spacetime and analyze how Yukawa corrections influence the resulting waveforms. In Sect. 7, we find the fundamental frequencies of the test particle and carry out the analysis of QPO phenomena using various precession models. Section 8 presents constraints on BH mass and Yukawa-type parameters within the framework of the RP model. Finally, we provide a brief conclusion to our results. Throughout the paper, we use the metric signature $(-,+,+,+)$ and units in which $G = c = 1$, unless stated otherwise.

2 The Einstein-nonlinear Maxwell–Yukawa metric

The ENLMY BH metric emerges from a spherically symmetric, static solution in $f(R)$ gravity, where the gravitational action is generalized by replacing the Ricci scalar R with an analytic function $f(R)$

$$\mathcal{A} = \frac{c^4}{16\pi G}\int d^4x\sqrt{-g}\,f(R) + \mathcal{L}_m, \tag{1}$$

choosing the special $f(R)$, which can be expressed in the form of a Taylor series, expanded around a fixed point R_0. In the weak-field limit, a Taylor expansion of $f(R)$ and truncation at leading order yields modified field equations as [56]

$$f(R) = \Sigma_n \frac{f^n(R_0)}{n!}(R-R_0)^n \approx f_0 + f_0' R + \frac{f_0''}{2}R^2 + ..., \tag{2}$$

where f_0 represents the cosmological constant, with $f_0' = 1$. This extended theory of gravity yields a solution characterized by a Yukawa-like potential, which represents a post-Newtonian correction to the Schwarzschild geometry [13]. This model is described by the metric given by [57,58]

$$\begin{aligned} ds^2 = &-[1+\Phi(r)]dt^2 + [1-\Phi(r)]dr^2 \\ &+r^2(d\theta^2 + \sin^2\theta d\phi^2), \end{aligned} \tag{3}$$

where

$$\Phi = -\frac{2M\left(\delta e^{-\frac{r}{\lambda}} + 1\right)}{(\delta+1)r}, \tag{4}$$

is known as a Yukawa-like potential. Here, δ and λ represent the coefficients of Taylor expansion, $f_0' = 1+\delta$, δ is a dimensionless parameter that characterizes the deviations from GR and governs the strength of the Yukawa-like correction, and $\delta = 0$ maps this metric to the Newtonian GR. Whereas $\lambda = [-f_0'/(6f_0'')]^{1/2}$, the parameter λ denotes a characteristic length scale that controls the exponential decay of the modification. In the limit $\delta = 0$, the potential reduces to the Newtonian potential, consistent with GR. The roots of the event horizon are given in Ref. [57]. They are found by solving $g_{tt}(r) = 0$, which leads to a transcendental equation due to the nonlinear nature of the Yukawa potential. Figure 1 shows the behavior of the Ricci scalar for different values of δ. The curvature increases near the horizon and decreases asymptotically with r.

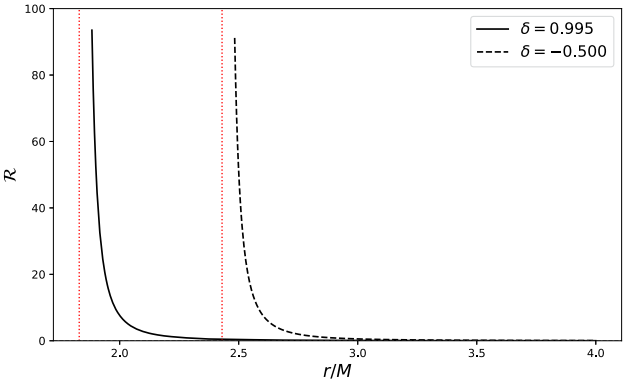

Fig. 1 Ricci scalar as a function of the radial coordinate r, plotted for two values of δ, with fixed $M = 1$ and $\lambda = 10$. Vertical red dotted lines mark the corresponding event horizons

3 Test particle dynamics around an ENLMY black hole

3.1 Equation of Motion

The static and spherically symmetric BH metric admits useful symmetries, namely, the time translation and spatial rotation about the symmetry axis. The associated conserved quantities can be determined using the Killing vectors [59], given respectively as

$$\xi^{\mu}_{(t)}\partial_\mu = \partial_t, \quad \xi^{\mu}_{(\phi)}\partial_\mu = \partial_\phi, \tag{5}$$

where $\xi^{\mu}_{(t)} = (1,\ 0,\ 0,\ 0)$ and $\xi^{\mu}_{(\phi)} = (0,\ 0,\ 0,\ 1)$. These symmetries give rise to conserved quantities: the specific energy $\mathcal{E} \equiv -p_\mu \xi^{\mu}_{(t)}/m$ and the specific azimuthal angular momentum $\mathcal{L}_z = \mathcal{L} \equiv p_\mu \xi^{\mu}_{(\phi)}/m$ of the moving particle. Therefore, we have

$$\dot{t} = \frac{\mathcal{E}}{1+\Phi(r)}, \quad \dot{\phi} = \frac{\mathcal{L}}{r^2\sin^2\theta}. \tag{6}$$

Here, an overdot denotes differentiation with respect to the proper time coordinate τ. To further investigate the geodesic motion, we adopt the Hamiltonian formalism $\mathcal{H} = \frac{1}{2}g^{\mu\nu}p_\mu p_\nu$ [60]; therefore, the Hamiltonian corresponding to our metric is

$$\mathcal{H} = \frac{1}{2}\left[-\frac{{p_t}^2}{[1+\Phi(r)]} + \frac{{p_r}^2}{[1-\Phi(r)]} + \frac{{p_\theta}^2}{r^2} + \frac{{p_\phi}^2}{r^2\sin^2\theta}\right], \tag{7}$$

and remains conserved along the particle's trajectory. In this framework, the cyclic nature of t and ϕ confirms the conservation of the conjugate momenta $p_t = -\mathcal{E}$ and $p_\phi = \mathcal{L}$, consistent with the Killing vector analysis. Using Hamilton's

equations $\dot{x}^\mu = \frac{\partial \mathcal{H}}{\partial p_\mu}$ and $\dot{p}_\mu = -\frac{\partial \mathcal{H}}{\partial x^\mu}$ [60], we obtain

$$\dot{p}_t = \dot{p}_\phi = 0, \quad \dot{r} = \frac{p_r}{[1-\Phi(r)]}, \quad \dot{\theta} = \frac{p_\theta}{r^2}. \tag{8}$$

By the normalization of the four-momentum, the Hamiltonian takes the fixed value $\mathcal{H} = \frac{1}{2} g^{\mu\nu} p_\mu p_\nu = \frac{1}{2}\epsilon$, with $\epsilon = -1$ for massive and $\epsilon = 0$ for massless particles. Therefore, we have

$$\dot{p}_r = \frac{1}{2}\left[-\frac{p_r^2}{[1-\Phi(r)]'} + \frac{2p_\theta^2}{r^3} - \frac{2\Theta}{r^3} + \partial_r\left(\frac{\mathcal{R}}{[1+\Phi(r)]}\right)\right], \tag{9}$$

$$\dot{p}_\theta = \frac{1}{2r^2}\partial_\theta\left(\Theta\right), \tag{10}$$

where "$\prime$" denotes differentiation with respect to the radial coordinate r, and

$$\mathcal{R}(r) = \mathcal{E}^2 - [1+\Phi(r)]\left(1 + \frac{\mathcal{L}^2}{r^2} + \frac{\mathcal{K}}{r^2}\right), \tag{11}$$

$$\Theta(\theta) = \mathcal{K} - \frac{\mathcal{L}^2\cos^2\theta}{\sin^2\theta}. \tag{12}$$

Here, $\mathcal{K}$ is the separation constant. Hereafter, the motion of the test particles at the equatorial plane will be considered a constant plane, choosing $\theta = \pi/2$ and $\mathcal{K} = 0$.

4 Effective potential and circular orbits

By applying the Hamiltonian constraint $g^{\mu\nu}p_\mu p_\nu = \epsilon$, the particle's trajectory can be analyzed using an effective potential V_{eff} through a corresponding first-order equation [22]. Therefore, we have [13]

$$\mathcal{E}^2 = \dot{r}^2[1-\Phi^2(r)] + V_{\text{eff}};$$
$$V_{\text{eff}} = [1+\Phi(r)]\left(1 + \frac{\mathcal{L}^2}{r^2}\right). \tag{13}$$

In Fig. 2, we analyze the effective potential of the radial motion of the test particles around the ENLMY BH for different values of the BH charge and the parameters λ and δ. As expected for an asymptotically flat spacetime, it is evident that $V_{\text{eff}} \to 1$ as $r \to \infty$. Consequently, particles with energy $\mathcal{E} > 1$ can escape to infinity, while those with $\mathcal{E} < 1$ remain gravitationally bound. Therefore, $\mathcal{E} = 1$ serves as the critical energy that separates bound and unbound orbits.

The motion of test particles in circular orbits can be studied by solving the equation $\partial_r V_{\text{eff}} = 0$, which gives the critical values of the angular momentum of the particles in the circular motion $\mathcal{L}_{\text{cr}} = \mathcal{L}$. To analyze circular motion, we consider the conditions under which the radial velocity vanishes, i.e., $\dot{r} = 0$, and there are no radial accelerations, $\ddot{r} = 0$. These

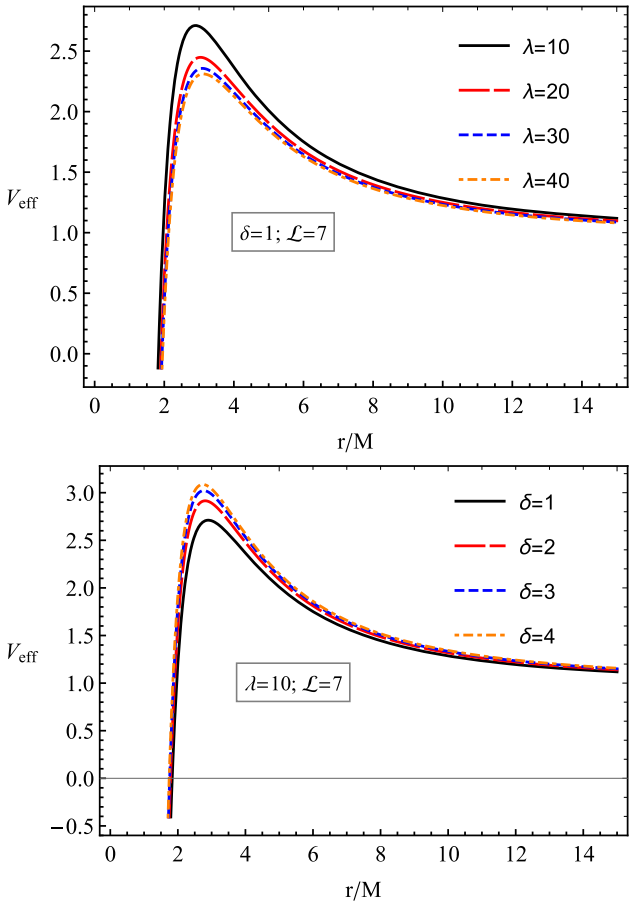

Fig. 2 Effective potential for radial motion of test particles around the ENLMY BH for various values of parameters λ and δ

conditions yield the radial profiles of the specific angular momentum and specific energy for particles in circular orbits confined to the equatorial plane ($\theta = \frac{\pi}{2}$), expressed as follows

$$\frac{\mathcal{L}^2}{M} = -\frac{Mr^2\left[\lambda\left(\delta + e^{r/\lambda}\right) + \delta r\right]}{\delta M(3\lambda + r) - \lambda e^{r/\lambda}(-3M + \delta r + r)}, \tag{14}$$

$$\frac{\mathcal{E}^2}{M} = \frac{\lambda e^{-\frac{r}{\lambda}}\left[e^{r/\lambda}(-2M + \delta r + r) - 2\delta M\right]^2}{(\delta+1)r\left[\lambda e^{r/\lambda}(-3M + \delta r + r) - \delta M(3\lambda + r)\right]}. \tag{15}$$

Figure 3 illustrates the radial dependence of the specific energy of particles in circular orbits around an ENLMY BH, showing how the energy profile varies with different values of λ and δ. It shows that increasing the Yukawa parameters λ and δ leads to a higher specific energy and shifts the location of the minimum energy (stable orbit) to larger radii.

In Fig. 4, we display the specific angular momentum of the particle corresponding to the circular motion as a function of the radial coordinate for different values of λ and δ. As the

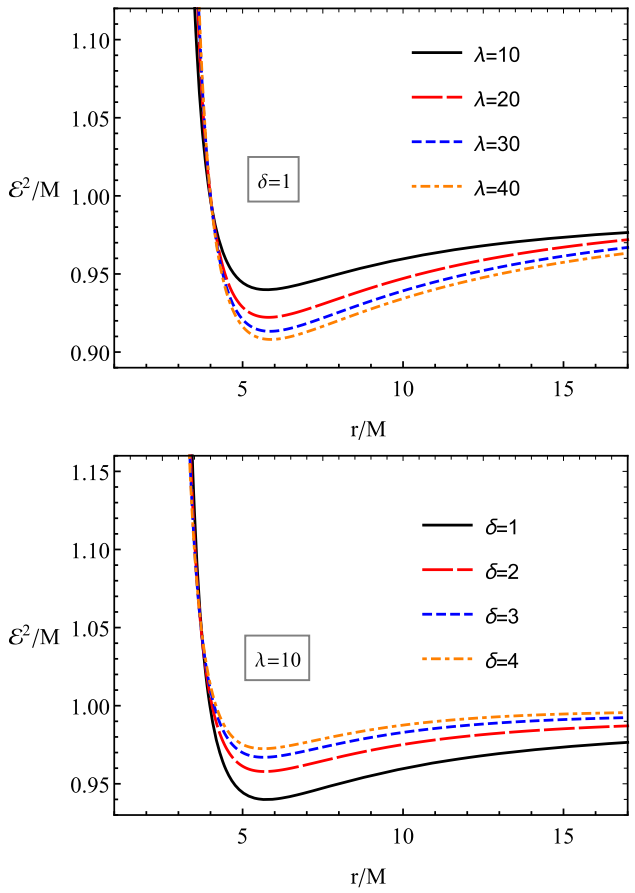

Fig. 3 The radial dependence of the specific energy of a particle in circular orbits around the ENLMY BH for different values of λ and δ

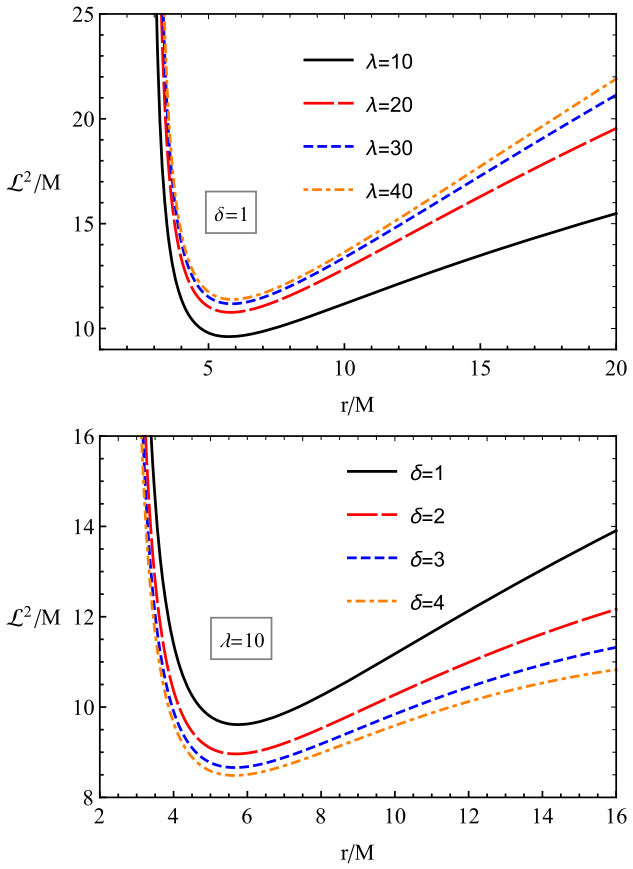

Fig. 4 The radial dependence of the specific angular momentum of a particle in circular orbits around the ENLMY BH for different values of λ and δ

Yukawa parameters λ and δ increase, the minimum of the angular momentum shifts to larger radii.

4.1 Innermost Stable and Innermost Bound Circular Orbits

To determine the radius of the ISCO, we begin with the radial equation of motion $\dot{r}^2 = \mathcal{E}^2 - V_{\text{eff}}(r)$. The ISCO defines the minimum radius at which a test particle can maintain a stable circular orbit around a massive object and is characterized by the following conditions [14,61,62]

$$\frac{dV_{\text{eff}}}{dr} = 0, \quad \frac{d^2V_{\text{eff}}}{dr^2} = 0, \quad V_{\text{eff}} = \mathcal{E}^2. \tag{16}$$

Applying these conditions leads to the following equation for the ISCO radius

$$\begin{aligned} &-2\delta^2 M\left(3\lambda^2 + r^2 + 5\lambda r\right) \\ &-\delta e^{r/\lambda}\Big[(\delta+1)r\left(-\lambda^2 + r^2 - \lambda r\right) \\ &-2M(r-6\lambda)(\lambda+r)\Big] + \lambda^2 e^{2r/\lambda}(-6M + \delta r + r) = 0. \end{aligned} \tag{17}$$

The IBCO represents the smallest unstable circular orbit with finite energy, specifically $\mathcal{E} = 1$. At this radius, a test particle has the same energy as it would have at infinity, indicating no energy loss during infall. Thus, the IBCO marks the threshold between bound and plunging orbits. For IBCO, the conditions for particle motion are [14,19,61]

$$\frac{dV_{\text{eff}}}{dr} = 0, \quad V_{\text{eff}} = \mathcal{E}^2 = 1. \tag{18}$$

Applying these conditions leads to the following equation for the IBCO radius

$$\begin{aligned} &\lambda e^{-\frac{r}{\lambda}}\left[e^{r/\lambda}(-2M + \delta r + r) - 2\delta M\right]^2 - (\delta+1)r \\ &\times\left[\lambda e^{r/\lambda}(-3M + \delta r + r) - \delta M(3\lambda + r)\right] = 0. \end{aligned} \tag{19}$$

The transcendental Eqs. (17) and (19) generally do not admit analytical solutions. However, for fixed values of the parameters λ and δ, the radii corresponding to the ISCO and

Table 1 Values of $r_{\rm ISCO}/M$, $r_{\rm IBCO}/M$, $\mathcal{L}_{\rm ISCO}/M$, and $\mathcal{L}_{\rm IBCO}/M$ for different values of δ, with fixed $\lambda = 10$ and $\lambda = 60$. Similar results are obtained for other values of λ

δ	$\lambda = 10$				$\lambda = 60$			
	$r_{\rm ISCO}$	$r_{\rm IBCO}$	$\mathcal{L}_{\rm ISCO}$	$\mathcal{L}_{\rm IBCO}$	$r_{\rm ISCO}$	$r_{\rm IBCO}$	$\mathcal{L}_{\rm ISCO}$	$\mathcal{L}_{\rm IBCO}$
−0.9	54.9635	35.6635	34.1538	39.1526	8.05754	4.87847	5.06249	7.41828
−0.8	14.2149	9.91364	12.4269	15.4844	6.77431	4.21682	4.02719	5.19746
−0.7	8.77196	5.96022	6.77339	8.83245	6.43011	4.08847	3.77128	4.65352
−0.6	7.39147	4.92928	5.16396	6.60944	6.27008	4.04298	3.65537	4.40733
−0.5	6.80445	4.50169	4.46530	5.57499	6.17758	4.02254	3.58926	4.26678
−0.4	6.48776	4.28236	4.08171	4.98607	6.11732	4.01211	3.54652	4.17582
−0.3	6.29269	4.15655	3.84063	4.60733	6.07493	4.00637	3.51663	4.11213
−0.2	6.16193	4.07968	3.67545	4.34351	6.04350	4.00307	3.49455	4.06502
−0.1	6.06899	4.03109	3.55533	4.14918	6.01926	4.00113	3.47756	4.02877
0.0	6.00000	4.00000	3.46410	4.00000	6.00000	4.00000	3.46410	4.00000
0.1	5.94705	3.98031	3.39248	3.88182	5.98432	3.99936	3.45317	3.97662
0.2	5.90533	3.96831	3.33476	3.78582	5.97132	3.99902	3.44411	3.95723
0.3	5.87173	3.96167	3.28727	3.70627	5.96036	3.99889	3.43648	3.94090
0.4	5.84418	3.95883	3.24751	3.63924	5.95090	3.99889	3.42997	3.92696
0.5	5.82125	3.95874	3.21373	3.58196	5.94289	3.99897	3.42434	3.91491
0.6	5.80191	3.96065	3.18469	3.53244	5.93582	3.99911	3.41944	3.90440
0.7	5.78541	3.96405	3.15944	3.48919	5.92960	3.99928	3.41513	3.89515
0.8	5.77120	3.96854	3.13730	3.45107	5.92408	3.99948	3.41130	3.88694
0.9	5.75886	3.97384	3.11720	3.41721	5.91914	3.99969	3.40788	3.87961

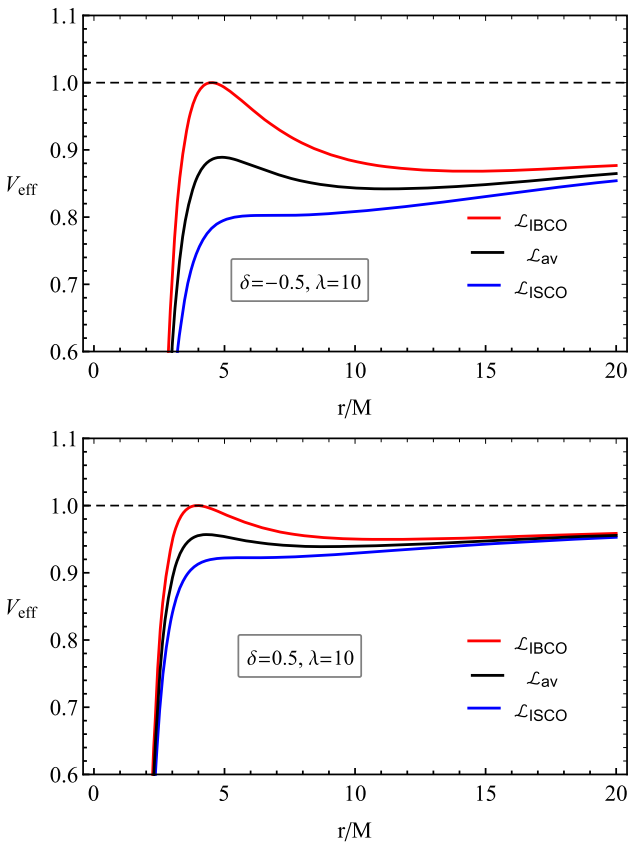

Fig. 5 Behavior of the effective potential for various angular momenta, plotted for $\lambda = 10$ and $\delta = -0.5$ (top), 0.5 (bottom)

IBCO can be determined numerically. To reduce the number of free parameters, we define a new angular momentum given as [19,63]

$$\mathcal{L}_{\rm av} = \frac{\mathcal{L}_{\rm ISCO} + \mathcal{L}_{\rm IBCO}}{2}. \tag{20}$$

For each chosen pair of λ and δ, one can uniquely determine $\mathcal{L}_{\rm ISCO}$ and $\mathcal{L}_{\rm IBCO}$, such that the angular momentum of the test particles satisfies the condition $\mathcal{L}_{\rm ISCO} < \mathcal{L}_{\rm av} < \mathcal{L}_{\rm IBCO}$ [19,63]. In Table 1, we present the values of the ISCO radius, the IBCO radius, $\mathcal{L}_{\rm ISCO}$, and $\mathcal{L}_{\rm IBCO}$ for various parameter sets. In Fig. 5, the effective potential is shown for different values of angular momentum. For $\mathcal{L}_{\rm IBCO}$, the maximum of the potential corresponds to $V_{\rm eff} = 1$ for all values of λ and δ.

5 Periodic orbits

In this section, we investigate the periodic orbits of test particles around the ENLMY BH, employing the classification scheme proposed by Levin [63]. Bound orbits are characterized by oscillations in both the radial coordinate r and the angular coordinate ϕ. A periodic orbit arises when the ratio of the angular to radial orbital frequencies, given by $q = \frac{\omega_\phi}{\omega_r}$, is a positive rational number. Under this condition, the particle's trajectory becomes closed, allowing it to return to its initial position after a finite interval, thereby repeating its

motion. The rational number q can be expressed in terms of three integers (z, w, v) given by

$$q = w + \frac{v}{z} = \frac{\Delta\phi}{2\pi} - 1, \tag{21}$$

where

$$\Delta\phi = 2\int_{r_-}^{r_+} \frac{\dot{\phi}}{\dot{r}}\, dr = 2\int_{r_-}^{r_+} \frac{\mathcal{L}}{r^2\sqrt{\frac{1}{1-\Phi^2(r)}\left[\mathcal{E}^2 - [1+\Phi(r)]\left(1+\frac{\mathcal{L}^2}{r^2}\right)\right]}} dr. \tag{22}$$

The triplet of integers (z, w, v) provides a geometric interpretation of the orbital structure: z denotes the number of "zooms," w indicates the number of "whirls," and v specifies the number of distinct "vertices." The radial motion is bounded between two turning points r_+ and r_-, which lie between the ISCO and the IBCO. These turning points can be found by solving the condition $\dot{r}^2 = 0$, where $r_\pm$ are the roots of the equation $\mathcal{E}^2 = V_{\text{eff}}$. From Eqs. (21) and (22), the rational number q becomes

$$q = \frac{1}{\pi}\int_{r_-}^{r_+} \frac{\mathcal{L}}{r^2\sqrt{\frac{1}{1-\Phi^2(r)}\left[\mathcal{E}^2 - [1+\Phi(r)]\left(1+\frac{\mathcal{L}^2}{r^2}\right)\right]}} dr - 1. \tag{23}$$

From Eq. (23), the rational number q depends on $\mathcal{E}$, $\mathcal{L}$, M, λ, and δ. If we further consider $\mathcal{L} = \mathcal{L}_{\text{av}}$, where $\mathcal{L}_{\text{av}}$ is a fixed value determined by the parameters M, λ, and δ, then the rational number q becomes dependent only on the orbital energy $\mathcal{E}$. Using Eq. (23), we construct Tables 2 and 3 for various values of δ with $\lambda = 10$ and $\lambda = 60$, respectively.

From this table, it is evident that for small values of λ (i.e., $\lambda = 10$, as presented in Table 2), the energy associated with periodic orbits around the ENLMY BH is higher than that of the corresponding orbits in the Schwarzschild spacetime, regardless of the sign of δ. In contrast, for larger values of λ (i.e., $\lambda = 60$, as presented in Table 3), the energy of periodic orbits in the ENLMY spacetime becomes lower than in the Schwarzschild case, for any value of δ, whether positive or negative. Therefore, the stronger gravitational binding in the presence of Yukawa corrections highlights the influence of modified gravity on orbital dynamics. Figure 6 illustrates the periodic orbits of massive particles lying between the ISCO and IBCO around the ENLMY BH for $\lambda = 60$ and $\delta = 0.5$. Each orbit, identified by a triplet of integers, corresponds to a distinct energy value. After detailed analysis, we conclude that periodic orbits in ENLMY BH exhibit qualitative similarities to those in Schwarzschild and Kerr spacetimes. However, the presence of Yukawa corrections significantly alters the orbital energy profiles and enhances gravitational binding.

Table 2 Energy values and corresponding angular momentum for periodic orbits with parameters $(z = 1, 2, 3, w = 1, v = 1)$ around the ENLMY BH for $\lambda = 10$ and various values of $\delta = 0, 0.1, 0.2, 0.3, 0.4, 0.5$

δ	$\mathcal{L}_{\text{av}}$	$\mathcal{E}_{(1,1,0)}$	$\mathcal{E}_{(2,1,1)}$	$\mathcal{E}_{(3,1,1)}$	$\mathcal{E}_{(4,1,1)}$
0	3.732055	0.966348	0.968214	0.967969	0.967758
0.1	3.63715	0.970087	0.969362	0.969833	0.969833
0.2	3.56029	0.969985	0.969883	0.969405	0.969917
0.3	3.49677	0.969986	0.969974	0.96909	0.969707
0.4	3.443375	0.969182	0.969859	0.969893	0.968156
0.5	3.397845	0.969953	0.969267	0.969956	0.969967

Table 3 Energy values and corresponding angular momentum for periodic orbits with parameters $(z = 1, 2, 3, w = 1, v = 1)$ around the ENLMY BH for $\lambda = 60$ and various values of $\delta = 0, 0.1, 0.2, 0.3, 0.4, 0.5$

δ	$\mathcal{L}_{\text{av}}$	$\mathcal{E}_{(1,1,0)}$	$\mathcal{E}_{(2,1,1)}$	$\mathcal{E}_{(3,1,1)}$	$\mathcal{E}_{(4,1,1)}$
0	3.732055	0.966348	0.968214	0.967969	0.967758
0.1	3.714895	0.959224	0.956707	0.959458	0.957118
0.2	3.70067	0.958138	0.959965	0.959514	0.959925
0.3	3.68869	0.959995	0.958101	0.95963	0.959914
0.4	3.678465	0.95996	0.958681	0.959698	0.959991
0.5	3.669625	0.959134	0.959865	0.959931	0.959926

6 Gravitational wave radiation from periodic orbits

In this section, we investigate the GW radiation emitted by periodic orbits of a test particle in the background of the ENLMY BH spacetime. We consider an EMRI system where the mass of the orbiting particle is negligible compared to that of the central BH (supermassive BH), allowing us to treat the particle as a perturbation to the ENLMY geometry. Under this approximation, when the energy $\mathcal{E}$ and angular momentum $\mathcal{L}$ of the particle vary slowly due to the emission of GW, the adiabatic approximation becomes valid. Through this approach, the slow drift in conserved quantities due to gravitational radiation can be traced, revealing how periodic orbits evolve. The transitions between these orbits correspond to the emission of gravitational radiation.

To compute the GWs emitted by periodic orbits around the ENLMY BH, we adopt the kludge waveform approach as described in [64]. In this method, the smaller object is treated

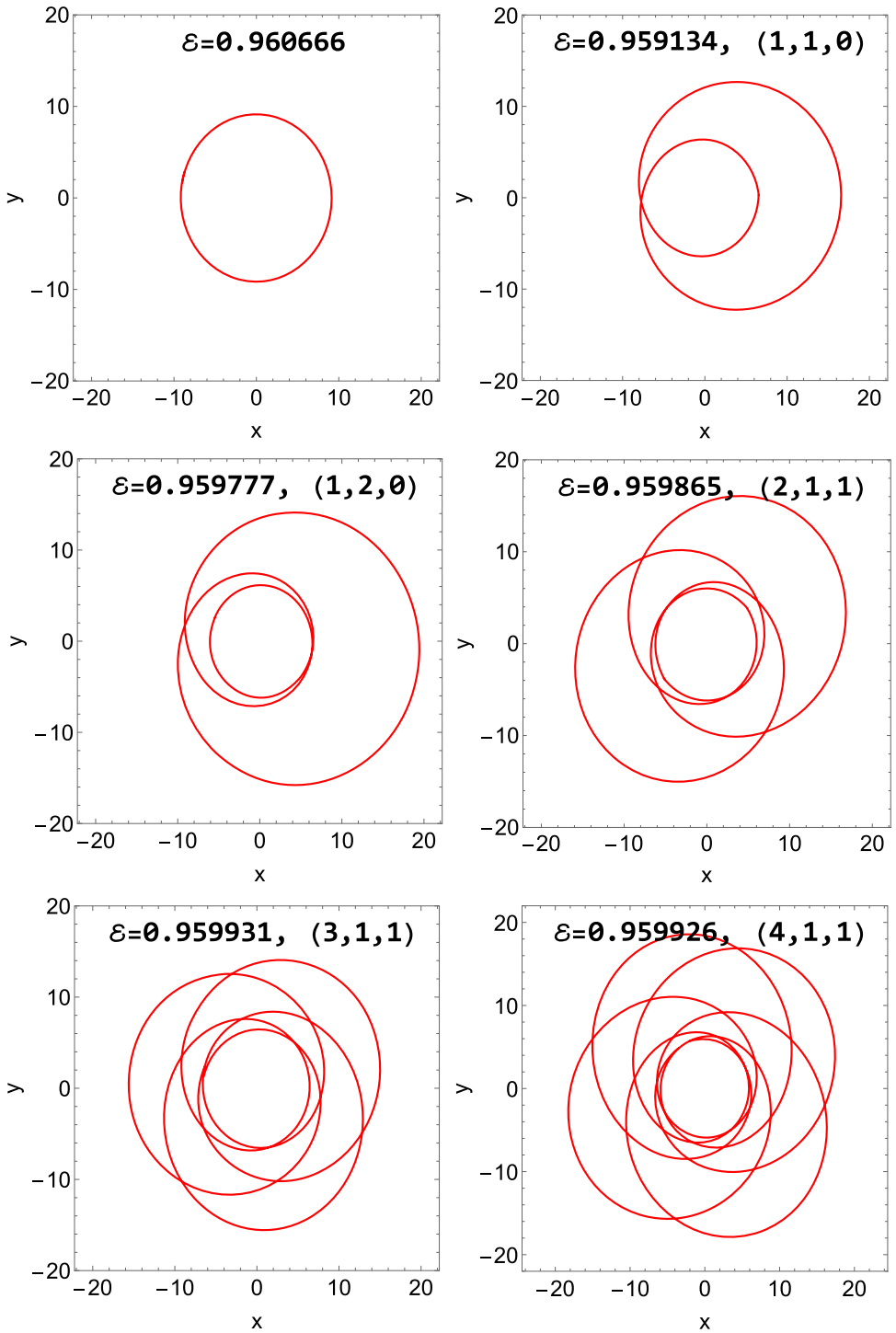

Fig. 6 Zoom-whirl periodic orbits for (z, w, v) with $z = 1, 2, 3, 4$, $w = 1, 2$, $v = 1$ for $\lambda = 60$ and $\delta = 0.5$, plotted using $x = \frac{r}{M}\cos\phi$, $y = \frac{r}{M}\sin\phi$

as a test particle moving in the fixed background of the BH. The periodic trajectories are first obtained by numerically solving the geodesic equations in the ENLMY spacetime. Once the orbital motion is determined, the GWs are computed using an approximate formula valid up to quadratic order [65–68]

$$h_{ij} = \frac{4\eta M}{D_L}\left(V_i V_j - \frac{m}{r}n_i n_j\right). \tag{24}$$

Here, M denotes the mass of the central ENLMY BH, m is the mass of the test particle, and D_L represents the luminosity distance to the EMRI system. The symmetric mass ratio is defined as $\eta = \frac{Mm}{(M+m)^2}$, while V_i refers to the spatial velocity components of the test particle. The vector n_i is the unit radial vector that points from the source to the observer, aligned with the direction of motion of the test particle. The resulting GW radiation can be projected onto a

detector-adapted coordinate system to yield the two polarization modes of the waveform, the plus (h_+) and cross ($h_\times$) polarizations, given by [65–68]

$$h_+ = -\frac{2\eta}{D_L}\frac{M^2}{r}\left(1+\cos^2\iota\right)\cos\left(2\phi+2\zeta\right), \tag{25}$$

$$h_\times = -\frac{4\eta}{D_L}\frac{M^2}{r}\cos\iota\sin\left(2\phi+2\zeta\right), \tag{26}$$

where ι denotes the inclination angle between the orbital angular momentum of the EMRI system and the observer's line of sight, while ζ represents the latitudinal viewing angle. To illustrate the GW waveforms produced by different periodic orbits and to investigate how the Yukawa-type corrections affect these signals, we consider an EMRI configuration in which the smaller body has mass $m \ll M$, with M being the mass of the central ENLMY BH. For simplicity, we fix the inclination and latitudinal angles to $\iota, \zeta = \frac{\pi}{4}$. The luminosity distance to the source is assumed to remain constant, with $D_L = 200Mpc$. Under these assumptions, the resulting waveforms are [19]

$$h_+ \propto -\frac{\cos(2\phi+2\zeta)}{r}, \tag{27}$$

and

$$h_\times \propto -\frac{\sin(2\phi+2\zeta)}{r}. \tag{28}$$

We restrict our analysis to plotting the right-hand sides of Eqs. (27) and (28) as functions of the coordinate time t.

In Figs. 7, 8, and 9, we consider small values of $|\delta| = 0.05$, focusing on periodic orbits and the corresponding GWs associated with the triplet of integers (3, 1, 1). In Figs. 10, 11, and 12, we consider small values of $|\delta| = 0.05$, focusing on periodic orbits and the corresponding GWs associated with the triplet of integers (4, 1, 1).

In Figs. 7-12, the periodic orbits, defined by a triplet of integers (z, w, v), exhibit distinct zoom and whirl phases within each complete cycle. During the zoom phase, the particle follows an extended, elliptical trajectory, moving away from the BH, where the gravitational field is relatively weaker. This motion corresponds to quieter segments in the GWs, observed in both h_+ and $h_\times$ polarizations, and aligns with the leaves of the orbit. As the particle spirals inward, it enters the whirl phase, tracing a tighter, nearly circular path in the strong-field region near the BH. This results in intense bursts in the GW signal due to the enhanced gravitational interaction. The number of quiet intervals corresponds to the number of leaves, while the louder bursts reflect the number of whirls; both features directly encode the orbital structure defined by the integer triplet.

In Figs. 7-12, the GW strains h_+ and $h_\times$ are shown normalized by 10^{-21}. Masses are converted from geometrized to SI units using $M \to \frac{GM}{c^2}$, introducing the overall factor $\frac{G^2}{c^4}$, and the luminosity distance D_L is converted from Mpc to meters ($1Mpc = 3.085677581 \times 10^{22}m$), with $G = 6.67430\times10^{-11}m^3kg^{-1}s^{-2}$ and $c = 2.99792458\times10^8 m/s$.

7 Fundamental Frequencies

The angular velocity/Keplerian frequency of the test particle, measured by a distant observer, is given by [69]

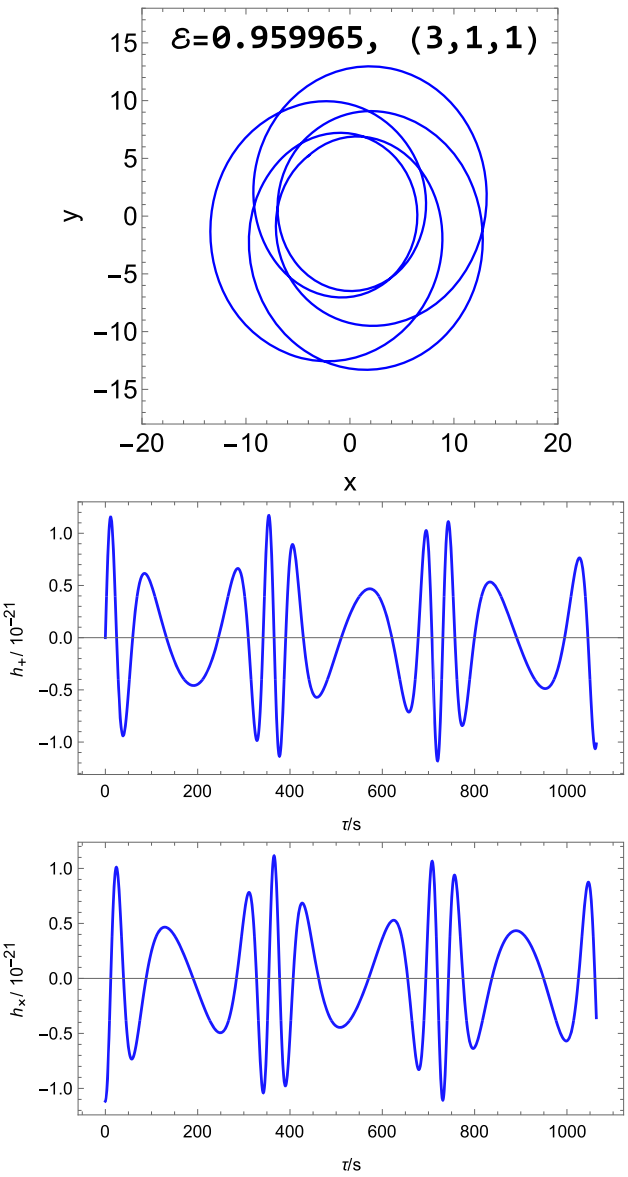

Fig. 7 The case $\delta = -0.05$, $\lambda = 60$, $\mathcal{L}_{\text{av}} = 3.742035$ and $\mathcal{E} = 0.959965$. The periodic orbit and the GW of the ENLMY BH for the triplet of integers (3, 1, 1)

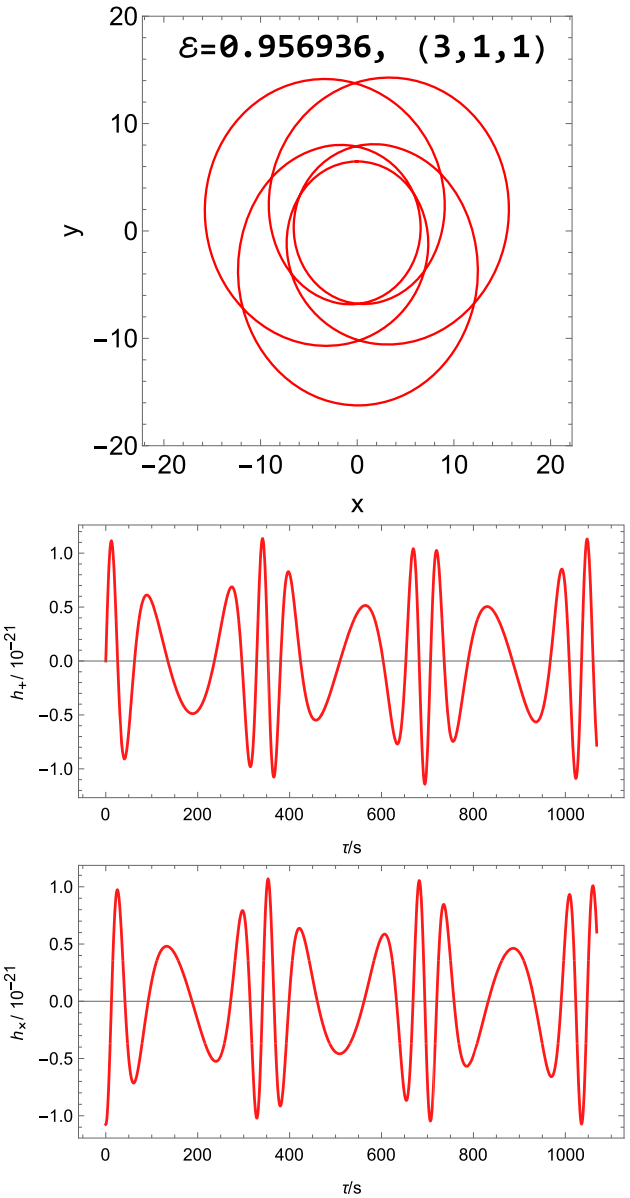

Fig. 8 The case $\delta = 0.05$, $\lambda = 60$, $\mathcal{L}_{\rm av} = 3.723045$ and $\mathcal{E} = 0.956936$. The periodic orbit and the GW of the ENLMY BH for the triplet of integers (3, 1, 1)

$$\Omega_K = \Omega_\phi = \frac{d\phi}{dt} = \frac{\dot{\phi}}{\dot{t}}\,. \tag{29}$$

For line element (3), the expression for the Keplerian frequency becomes

$$\Omega_\phi = \frac{\sqrt{M}e^{-\frac{r}{2\lambda}}\sqrt{\lambda\left(\delta + e^{r/\lambda}\right) + \delta r}}{\sqrt{\delta+1}\sqrt{\lambda}r^{3/2}}, \tag{30}$$

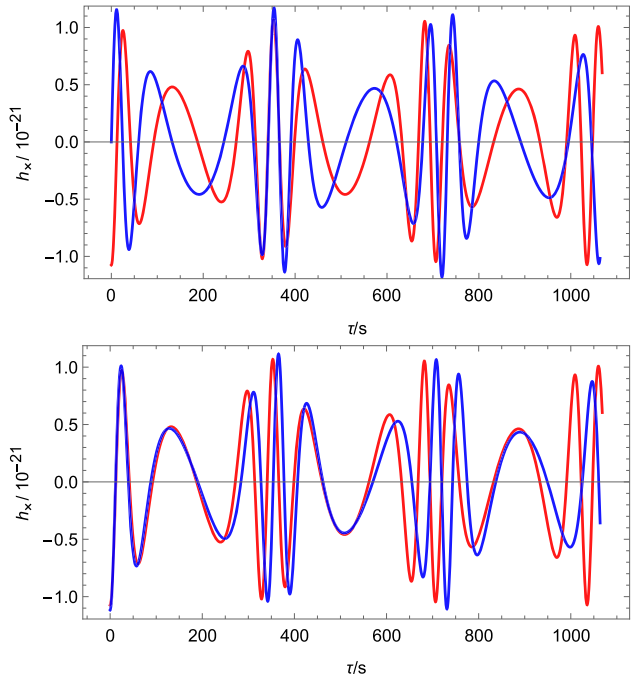

Fig. 9 Upper Panel: Combination of the plots of h_+ in Figs. 7 and 8. Lower Panel: Combination of the plots of $h_\times$ in Figs. 7 and 8

afterward

$$\Omega_\theta^2(r_0) = \Gamma^\theta_{\phi\phi,\theta}\left(u^\phi\right)^2,$$
$$\Omega_r^2(r_0) = \left(\Gamma^r_{jl,r} - 4\Gamma^r_{jk}\Gamma^k_{rl}\right)u^j u^l, \quad (j,k,l = t,\phi). \tag{31}$$

For spherically symmetric, non-rotating spacetimes, the expressions for $\Omega_r^2(r_0)$ can be expanded as

$$\Omega_r^2(r_0) = \left(\Gamma^r_{tt,r} - 4\Gamma^r_{tt}\Gamma^t_{rt}\right)\left(u^t\right)^2 + \left(\Gamma^r_{\phi\phi,r} - 4\Gamma^r_{\phi\phi}\Gamma^\phi_{r\phi}\right)\left(u^\phi\right)^2. \tag{32}$$

To express the fundamental frequencies ν_r and ν_θ in terms of the coordinate time t, we use

$$\nu_i = \frac{\Omega_i}{2\pi}\frac{d\tau}{dt}, (i = r,\theta). \tag{33}$$

For line element (3), we can write the fundamental frequencies of the radial and vertical oscillation of the test particle moving along the circular orbits around an ENLMY BH as

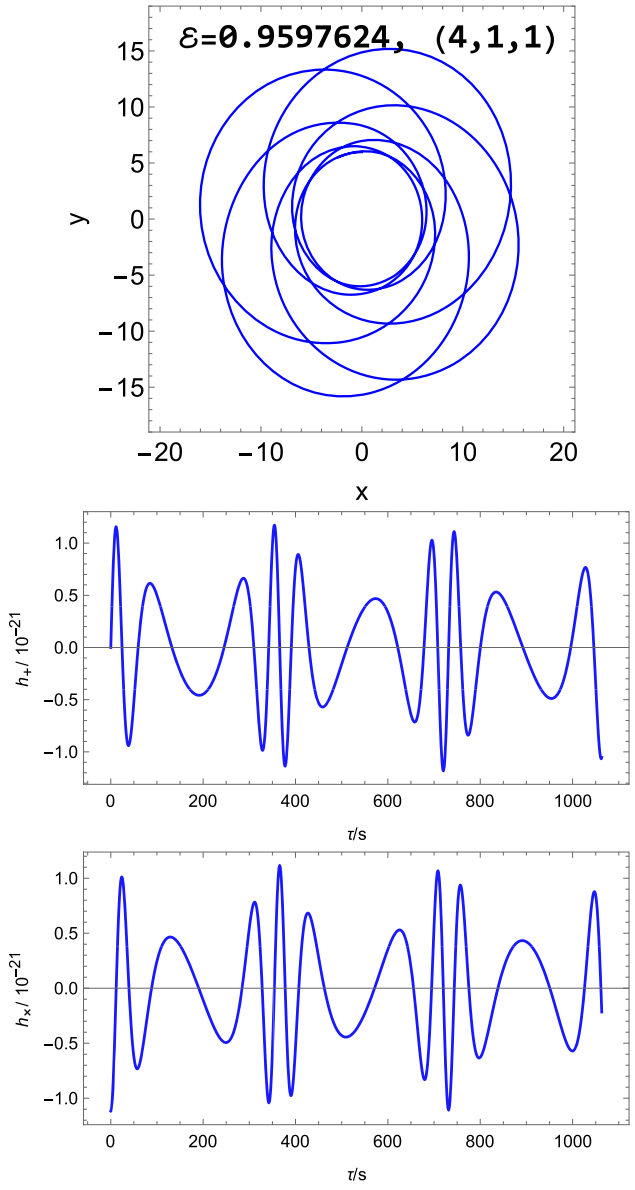

Fig. 10 The case $\delta = -0.05$, $\lambda = 60$, $\mathcal{L}_{\rm av} = 3.742035$ and $\mathcal{E} = 0.9597624$. The periodic orbit and the GW of the ENLMY BH for the triplet of integers (4, 1, 1)

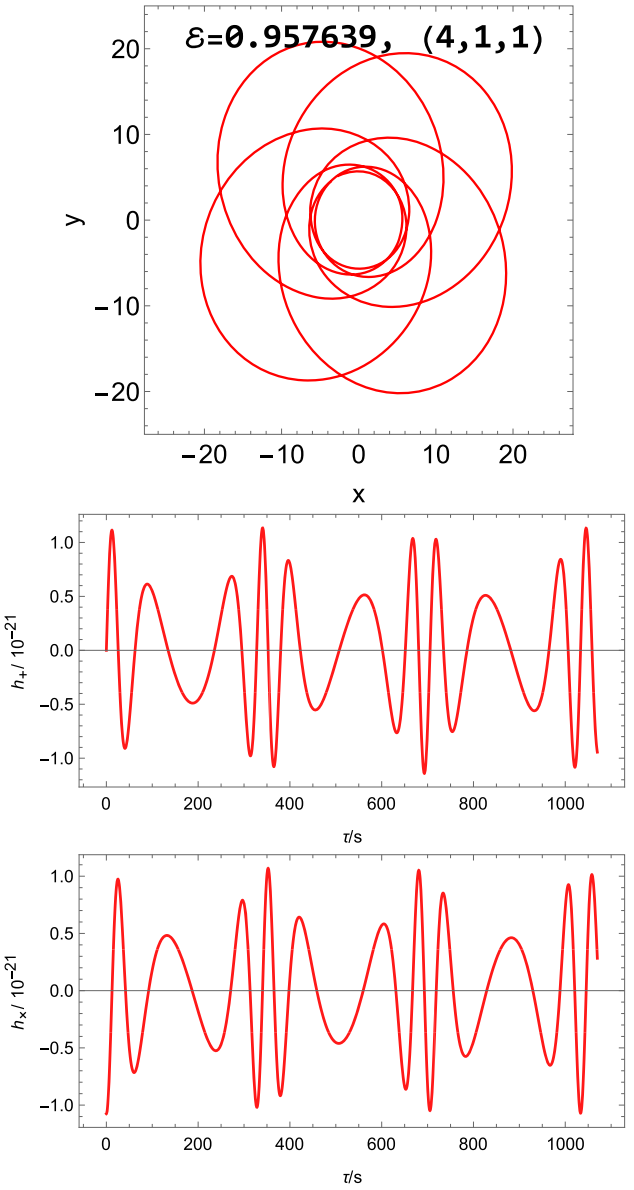

Fig. 11 The case $\delta = 0.05$, $\lambda = 60$, $\mathcal{L}_{\rm av} = 3.723045$ and $\mathcal{E} = 0.957639$. The periodic orbit and the GW of the ENLMY BH for the triplet of integers (4, 1, 1)

$$\left(\frac{\nu_r}{\nu_\phi}\right)^2 = \frac{(\delta+1)re^{r/\lambda}\left(\lambda^2 e^{\frac{2r}{\lambda}}(r-6M+\delta r-2\delta^2 M(3\lambda^2+r^2+5\lambda r)-\delta e^{r/\lambda}\left((\delta+1)r(-\lambda^2+r^2-\lambda r)-2M(r-6\lambda)(\lambda+r)\right)\right)}{\lambda\left(\lambda(\delta+e^{r/\lambda})+\delta r\right)\left(-4\delta^2M^2+e^{\frac{2r}{\lambda}}\left((\delta+1)^2r^2-4M^2\right)-8\delta M^2 e^{r/\lambda}\right)}, \tag{34}$$

and

$$\nu_\theta = \nu_\phi = \frac{1}{2\pi}\frac{\sqrt{M}e^{-\frac{r}{2\lambda}}\sqrt{\lambda\left(\delta+e^{r/\lambda}\right)+\delta r}}{\sqrt{\delta+1}\sqrt{\lambda}r^{3/2}}, \tag{35}$$

where $\nu_\phi = \frac{\Omega_\phi}{2\pi}$. We can observe that $\nu_\theta = \nu_\phi$, as the spacetime is non-rotating.

In Figs. 13 and 14, we have plotted the fundamental frequencies against r after converting the geometrical units into Hertz by using the factor $\frac{c^3}{GM}$, where the speed of light $c = 3 \times 10^{10}\,$cm/s and the gravitational constant $G = 6.67 \times 10^{-8}\,\mathrm{cm^3\,g^{-1}\,s^{-2}}$ [70,71]. We can note that $\nu_r|_{r=r_{\rm ISCO}} = 0$, indicating that for $r < r_{\rm ISCO}$, radial perturbations no longer produce oscillations but instead cause the orbit to become unstable.

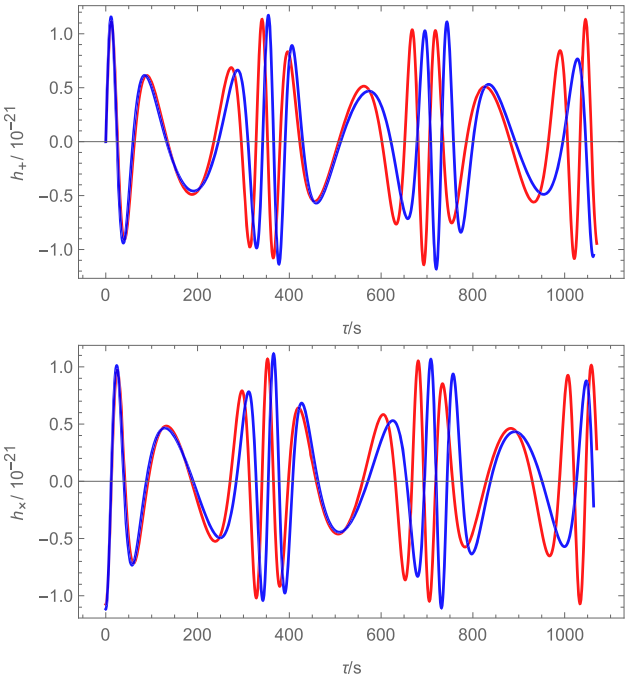

Fig. 12 Upper panel: Combination of the plots of h_+ in Figs. 10 and 11. Lower panel: Combination of the plots of $h_\times$ in Figs. 10 and 11

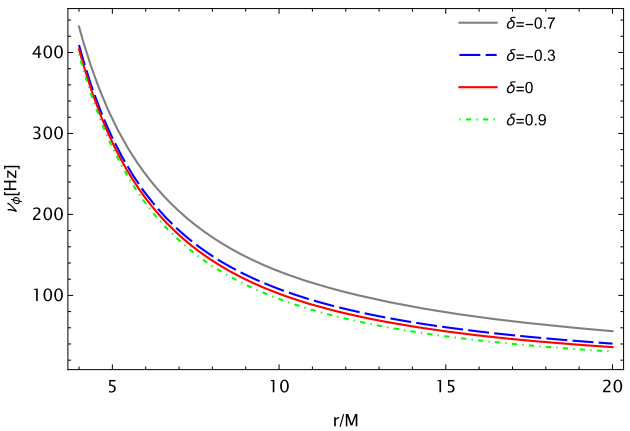

Fig. 13 ν_ϕ is plotted for different values of δ and $\lambda = 10$ by considering an object with mass $M = 10M_\odot$. The Schwarzschild case corresponding to $\delta = 0$ is given in red

7.1 Quasi-Periodic Oscillation Frequencies

In this subsection, we analyze the behavior of twin-peak QPO frequencies around an ENLMY BH, compare them with the Schwarzschild case, and discuss the relationship between the possible upper (ν_U) and lower (ν_L) QPO frequencies within three theoretical frameworks: the RP model ($\nu_U = \nu_\phi$ and $\nu_L = \nu_\phi - \nu_r$), the WD model ($\nu_U = 2\nu_K - \nu_r$ and $\nu_L = 2(\nu_K - \nu_r)$), and the TD model ($\nu_U = \nu_K + \nu_r$ and $\nu_L = \nu_K$) [72–75]. By comparing predictions for ENLMY and Schwarzschild BHs, we identify characteristic signatures

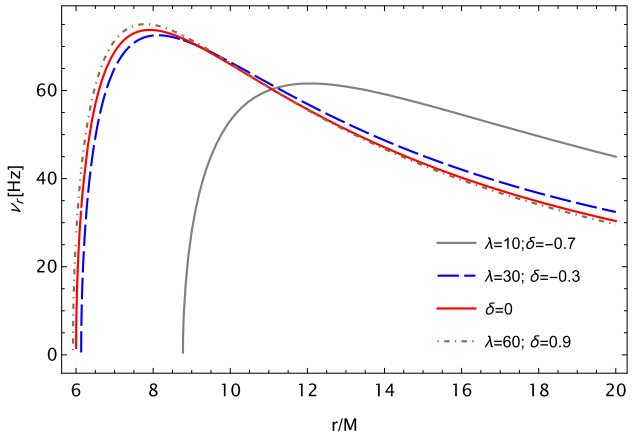

Fig. 14 We have considered an object with mass $M = 10M_\odot$. ν_r are plotted for different values of δ and λ. We can observe that it vanishes at $r = r_{\rm ISCO}$. The Schwarzschild case corresponding to $\delta = 0$ is given in red

that may distinguish between standard and modified gravity scenarios.

Figure 15 presents our results, showing the relationship between (ν_U) and (ν_L) QPO frequencies for each model under different parameter values of λ and δ. For numerical calculations, we fix the BH mass at $M = 10\,M_\odot$. In each model, the region between the ENLMY and Schwarzschild curves represents possible observational outcomes for twin-peak QPOs. For all three models considered, we observe that at a fixed value of $\lambda = 10$, the curves tend to converge within a certain intermediate region of the radial coordinate. In this region, the influence of the deformation parameter becomes negligible, and the models closely mimic the behavior of the Schwarzschild geometry. This "mimic region" is a common feature across all models and reflects a zone where modifications to GR are effectively suppressed. Furthermore, when λ is increased to $\lambda = 30$, we find that this mimic region becomes more extended. This indicates that a larger characteristic length scale λ allows the exponential corrections to decay more gradually, resulting in the models resembling Schwarzschild behavior over a wider radial domain.

Yukawa corrections are most relevant in strong fields, where deviations from GR are observed in QPO signals. Micro-quasars and galactic centers are therefore an alternative for probing ENLMY gravity through high-frequency oscillations.

8 MCMC analyses

This section is devoted to obtaining constraints on the BH mass and Yukawa parameters δ and λ. Here, we select three different BH candidates, namely stellar-mass, intermediate-mass, and supermassive BHs, in different objects, such as

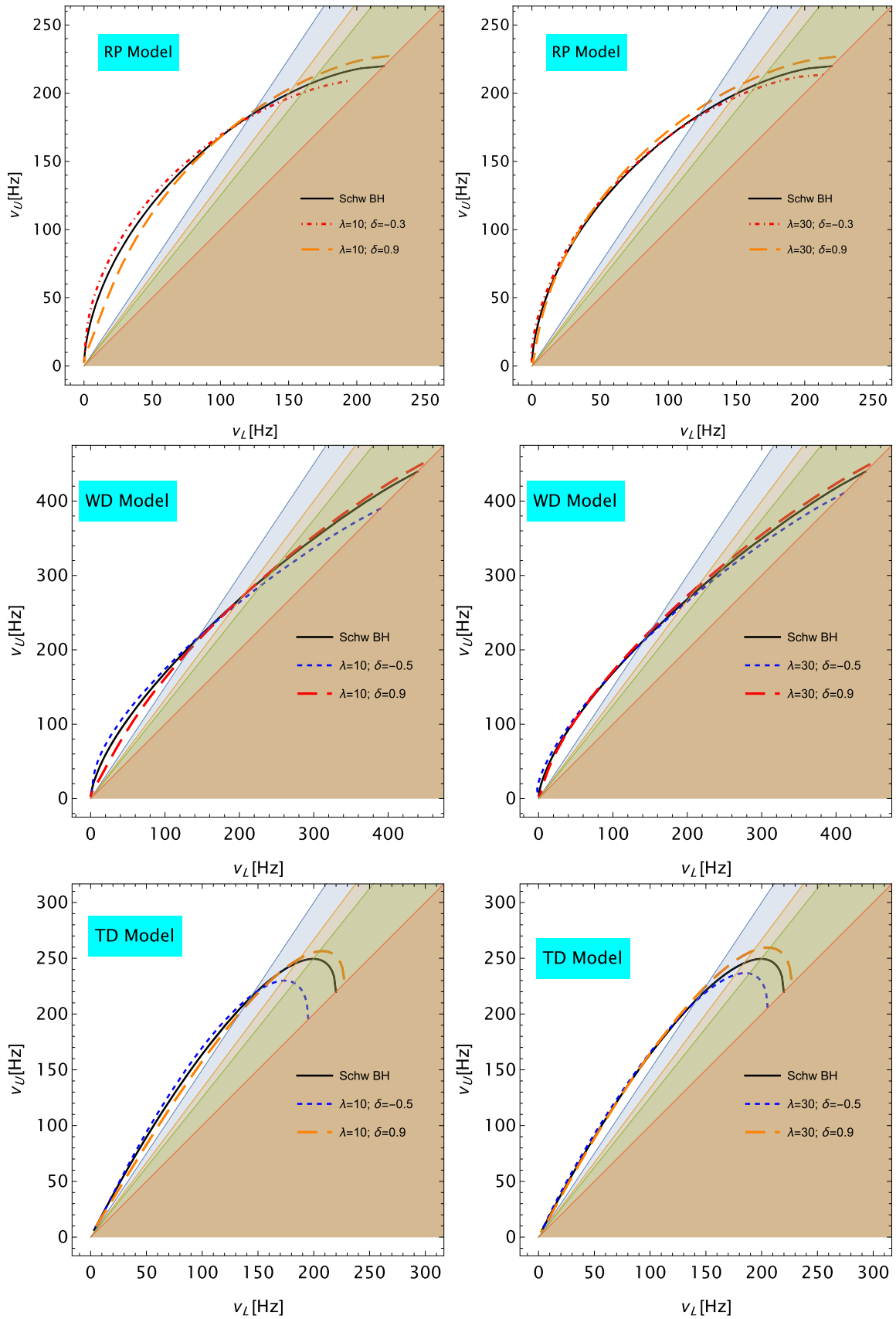

Fig. 15 Relations between the frequencies of upper and lower picks of twin-pick QPOs in the RP, WD, and TD models

Table 4 QPOs frequencies observed in microquasars and galactic center

Source	ν_U [Hz]	$\Delta\nu_U$ [Hz]	ν_L [Hz]	$\Delta\nu_L$ [Hz]	Mass [$M_\odot$]
XTE J1550-564 [84]	276	± 3	184	± 5	$12.4^{+2.0}_{-1.8}$
GRO J1655–40 [85]	451	± 5	298	± 4	5.4 ± 0.3
GRS 1915+105 [86]	168	± 3	113	± 5	$12.4^{+2.0}_{-1.8}$
M82 X-1 [76]	5.07	± 0.06	3.32	± 0.06	415 ± 63
Sgr A* [87]	1.445	± 0.16 mHz	0.886	± 0.04 mHz	$(4.1 \pm 0.6) \times 10^6$

Table 5 The Gaussian prior of BH spacetime in EU from QPOs for the microquasars and galactic centers

P	XTE J1550-564		GRO J1655-40		GRS 1915+105		Sgr A^*		M82 X-1	
	μ	σ	μ	σ	μ	σ	μ	σ	μ	σ
$M/M_\odot$	12.09	1.03	5.39	0.17	12.51	1.10	3.82×10^6	0.25×10^6	416.23	22.79
δ	0.66	0.24	0.61	0.24	0.61	0.24	0.83	0.13	0.61	0.23
λ	0.46	0.29	0.61	0.41	0.59	0.39	0.21	0.09	0.61	0.39
r	4.03	0.38	4.69	0.37	5.16	0.39	3.44	0.24	5.04	0.39

stellar mass BHs, which are located at the center of the microquasars GRO J1655-40, XTE 1550-564, and GRS 1915+105. We also use QPO data from M82 X-1 [76,77], an intermediate-mass BH at the ultraluminous X-ray source in galaxy M82. Its mass is estimated to be around 400 to 900 solar masses in the literature [78–83]. A supermassive BH, Sgr A*, is also in our focus with milliHertz QPOs. The QPO data of the objects are given in Table 4.

To estimate the four parameters as the QPO frequencies observed in the microquasars, we perform χ^2 analysis with [52]:

$$\begin{aligned}\chi^2(M,\delta,\lambda,r) &= \frac{(\nu_{1\phi}-\nu_{1U})^2}{\sigma_{1U}^2}+\frac{(\nu_{1per}-\nu_{1L})^2}{\sigma_{1L}^2}\\ &+\frac{(\nu_{1nod}-\nu_{1C})^2}{\sigma_{1C}^2}+\frac{(\nu_{2\phi}-\nu_{2U})^2}{\sigma_{2U}^2}\\ &+\frac{(\nu_{2nod}-\nu_{2C})^2}{\sigma_{2C}^2}\,. \end{aligned} \tag{36}$$

The best-estimated values of the parameters M, δ, λ, and r (radius of QPO orbits) are those in which $\chi^2_{\rm min}$ take the minimum. The range of parameters at the confidence level (C.L.) can be determined in the interval $\chi^2_{\rm min} \pm \Delta\chi^2$. To find these best-estimated values, we minimize χ^2 and obtain the following mean values for M, δ, λ, and r in Table 5.

We used the Python library `emcee` [88,89] to perform the MCMC analysis and constrain the parameters of the particle around an ENLMY BH. Our analysis used the relativistic precision (RP; see Sect. 7) method.

The posterior distribution can be defined as follows [90]:

$$\mathcal{P}(\theta|\mathcal{D},\mathcal{M}) = \frac{P(\mathcal{D}|\theta,\mathcal{M})\,\pi(\theta|\mathcal{M})}{P(\mathcal{D}|\mathcal{M})}, \tag{37}$$

where $\pi(\theta)$ is the prior and $P(D|\theta, M)$ is the likelihood. We choose our priors to be (normal) Gaussian within suitable boundaries (see Table 5), i.e., $\pi(\theta_i) \sim \exp\left[\frac{1}{2}\left(\frac{\theta_i-\theta_{0,i}}{\sigma_i}\right)^2\right]$, $\theta_{{\rm low},i} < \theta_i < \theta_{{\rm high},i}$. In this work, the parameters are $\theta_i = \{M, \delta, \lambda, r/M\}$, and σ_i are their corresponding variances. Following the orbital, periastron precession frequencies from Sect. 7, different parts of the data are used in our MCMC analysis. Eventually, the likelihood function Λ can be expressed as

$$\log\Lambda = \log\Lambda_U + \log\Lambda_L, \tag{38}$$

where $\log\Lambda_U$ denotes the likelihood of the astrometric upper/orbital frequencies,

$$\log\Lambda_U = -\frac{1}{2}\sum_i \frac{\left(\nu^i_{\phi,\rm obs}-\nu^i_{\phi,\rm th}\right)^2}{\left(\sigma^i_{\phi,\rm obs}\right)^2} \tag{39}$$

and $\log\Lambda_L$ represents the probability (likelihood) of the data for the lower or periastron precession frequency ($\nu_{\rm per}$),

$$\log\Lambda_L = -\frac{1}{2}\sum_i \frac{\left(\nu^i_{\rm per,obs}-\nu^i_{\rm per,th}\right)^2}{\left(\sigma^i_{\rm per,obs}\right)^2}. \tag{40}$$

Here, $\nu^i_{\phi,\rm obs}$ and $\nu^i_{\rm per,obs}$ are observational results of the orbital/Keplerian frequencies (ν_K), periastron precession frequencies $\nu_{\rm per} = \nu_K - \nu_r$ for the sources mentioned above. On the other side, $\nu^i_{\phi,\rm th}$, $\nu^i_{\rm per,th}$ are the respective theoretical estimations.

Next, we perform the MCMC simulation to constrain the parameters $(M, \delta, \lambda, r/M)$ for an ENLMY BH. We use Gaussian priors based on parameter values from the existing lit-

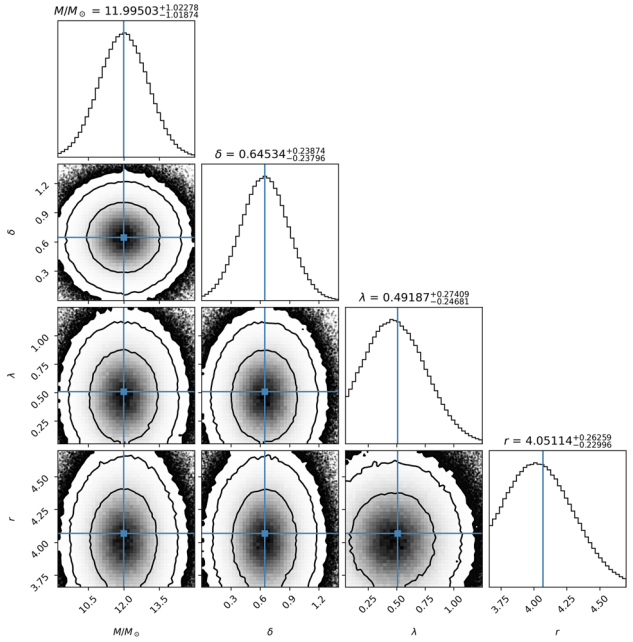

Fig. 16 Constraints on the Yukawa parameters, the BH mass, and the radius of the QPO orbit from a four-dimensional MCMC analysis using the QPO data for the stellar-mass BH XTE J1550-564 in the RP model

erature on QPO data processing. We sampled approximately 10^5 points for each parameter from a Gaussian prior distribution, allowing us to explore the physically possible parameter space within set boundaries and identify the best-fitting parameter values.

Now, we collect the best-fit values for the parameters (M, δ, λ, r) obtained from the MCMC results in Figs. 16 and 17 and present them in table form.

Our estimated masses exhibit minor deviations relative to the limits reported in our earlier study, as well as to those presented in other works [91–100]. The oscillation frequencies depend not only on the BH mass but also on the gravity parameters, in particular, the Yukawa δ and λ parameters. Therefore, the results of the constraint with the QPO frequencies should also differ for each case.

9 Conclusion

In this paper, we investigated the motion of test particles around the ENLMY BH, a modified spacetime arising from $f(R)$ gravity coupled with nonlinear electrodynamics and Yukawa-type corrections. Beginning with the analysis of the spacetime metric and its associated symmetries, we derived the equations of motion using the Hamiltonian formalism. By exploiting the conserved quantities associated with Killing vectors, we investigated the dynamics of particles confined to the equatorial plane, enabling us to simplify and understand the behavior of geodesic motion under the influence of the Yukawa potential.

Our analysis of the effective potential revealed critical insights into the structure of circular orbits. We derived expressions for the specific energy and angular momentum of particles in stable circular motion and identified the locations of the ISCO and IBCO. These orbits are sensitive to the Yukawa parameters λ and δ, with increasing values that shift the ISCO and IBCO to larger radii, requiring higher energy and angular momentum for circular motion. Through numerical analysis, we showed how these parameters affect the structure of bound orbits and presented detailed profiles of the effective potential and its dependence on the spacetime deformation.

Furthermore, we explored periodic orbits using Levin's classification scheme [63,101], characterizing them by the rational number q, which is dependent on the energy, angular momentum, and spacetime parameters λ and δ. Our results reveal that the orbital dynamics around the ENLMY BH are strongly influenced by the Yukawa parameters λ and δ. For small values of λ, the energy required for periodic orbits in the ENLMY spacetime is generally higher than that in the Schwarzschild case, regardless of the sign of δ. However, as λ increases, the energy of periodic orbits becomes lower than that of the Schwarzschild counterpart for both positive and negative δ. This behavior indicates that Yukawa corrections can either weaken or strengthen the gravitational binding depending on the parameter regime, thereby modifying the conditions for closed orbits and enriching the structure of the orbital phase space.

Additionally, we analyzed the GW radiation emitted by periodic orbits characterized by different (z, w, v) configurations in the ENLMY spacetime. The resulting waveforms for the plus (h_+) and cross $(h_\times)$ polarizations display characteristic zoom-whirl structures, as illustrated in Figs. 7-12. Specifically, the waveforms exhibit quiet phases during the extended zoom segments of the orbit and sharp, high-amplitude glitches during the rapid whirl phases. The number of these glitches corresponds directly to the number of whirls in each orbit, while the quiet intervals align with the orbital leaves. These waveform patterns reflect the impact of the Yukawa parameters λ and δ on the GW phase evolution, indicating how modifications to the gravitational potential affect orbital dynamics. Such distinctive features in the GW signal offer promising observational signatures that may serve to test and constrain the ENLMY BH model with upcoming GW detectors.

We determined the fundamental frequencies of a test particle using the perturbed geodesic equation in the vicinity of a circular orbit. We observed that as r decreases, the radial fundamental frequency increases, attains a certain peak, and then starts decreasing. Eventually, it vanishes at the radius of ISCO. We also analyzed the twin-peak QPO frequencies for

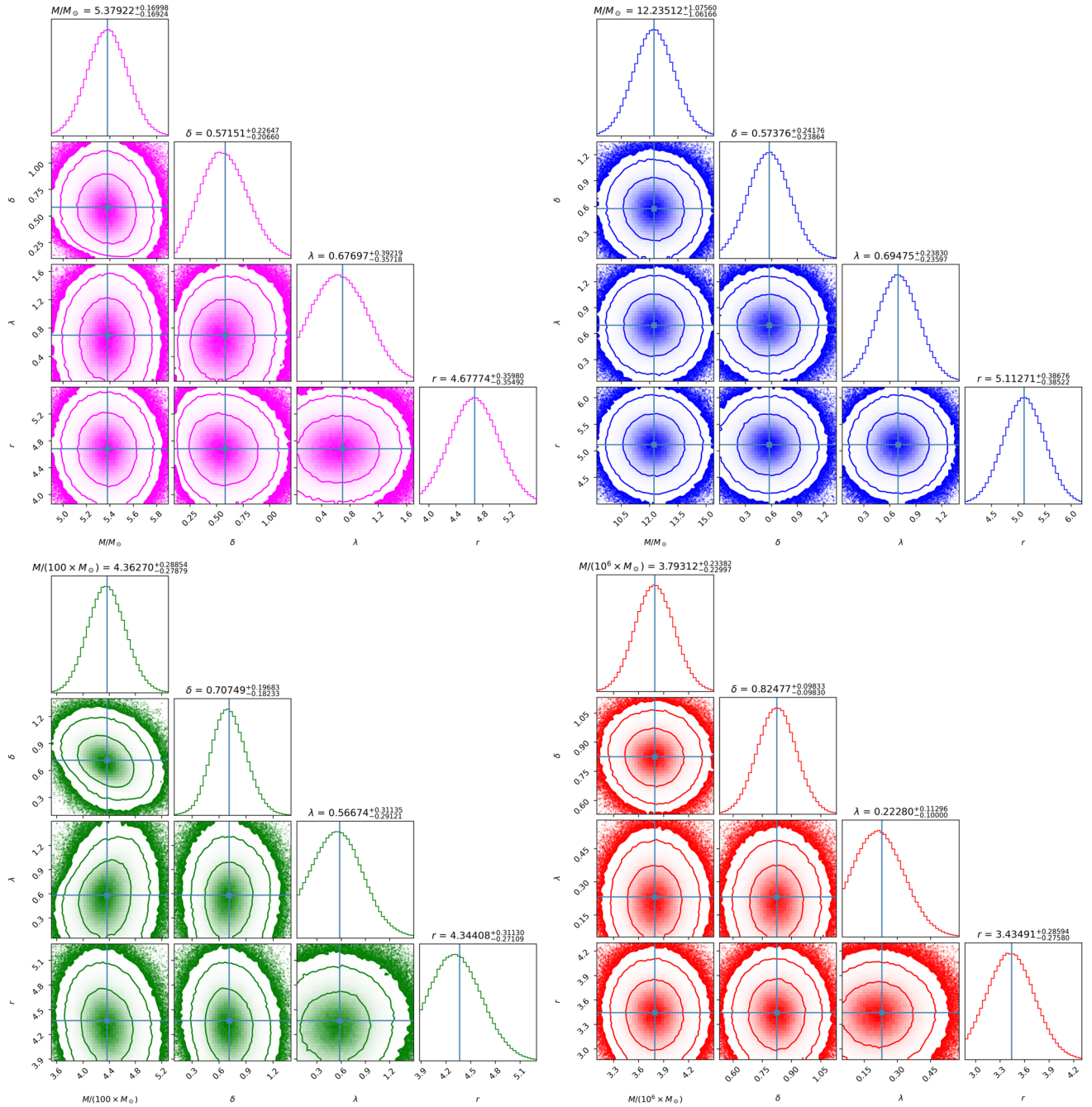

Fig. 17 The same constraints and values as those shown in Fig. 16, but for GRO J1655-40 (in the top-left panel with magenta) and GRS 1915+105 (in the top-right panel with blue), M82 X-1 (in the bottom-left panel with green), and Sgr A* (in the bottom-right panel with red)

Table 6 The best-fit values of the BH in ENLMY spacetime

P	XTE J1550-564	GRO J1655-40	GRS 1915+105	M82 X-1	Sgr A^*
$M/M_\odot$	$11.995^{+1.028}_{-1.018}$	$5.379^{+0.169}_{-0.169}$	$12.235^{+1.075}_{-1.061}$	$4.362^{+0.288}_{-0.278} \times 10^2$	$3.793^{+0.233}_{-0.229} \times 10^6$
δ	$0.645^{+0.238}_{-0.237}$	$0.571^{+0.226}_{-0.206}$	$0.573^{+0.241}_{-0.238}$	$0.707^{+0.196}_{-0.182}$	$0.824^{+0.098}_{-0.098}$
λ	$0.491^{+0.274}_{-0.229}$	$0.676^{+0.392}_{-0.357}$	$0.694^{+0.238}_{-0.235}$	$0.566^{+0.311}_{-0.291}$	$0.223^{+0.112}_{-0.100}$
r/M	$4.052^{+0.268}_{-0.230}$	$4.677^{+0.392}_{-0.357}$	$5.112^{+0.386}_{-0.385}$	$4.344^{+0.311}_{-0.271}$	$3.435^{+0.285}_{-0.275}$

three models and observed that increasing the characteristic length scale increases the mimic region. This is because a larger length scale means that the deviations from GR are weaker, and so the behavior of the BH becomes more similar to the Schwarzschild case over a wider range of radii. Hence, we can say that astrophysical observations may not easily distinguish between modified gravity and GR. Consequently, high-precision observations could be employed to place meaningful constraints on the allowed values of λ.

Finally, in the last section, we provided MCMC analyses to obtain constraints on the ENLMY BH mass parameters. We chose data from QPOs observed in X-ray binaries: GRO J1655-40, GRS 1915-105, and XTE J1550-564. Details of the MCMC analyses are shown in Figs. 16 & 17, and best values are provided in Table 6.

In summary, the ENLMY black hole provides a natural testing ground for probing intermediate-scale deviations from GR. By combining QPO data with gravitational wave signatures, one can place observational constraints on the Yukawa parameters. This strongly motivates future observations to distinguish ENLMY gravity from other beyond-GR frameworks.

Funding No organization supported this research financially.

Data Availability Statement This manuscript has no associated data. [Authors' comment: Data sharing not applicable to this article as no datasets were generated or analysed during the current study.]

Code Availability Statement This manuscript has no associated code/software. [Authors' comment: Code/Software sharing not applicable to this article as no code/software was generated or analysed during the current study.]

Funded by SCOAP[3].

References

1. F. Dyson, A. Eddington, C. Davidson, A determination of the deflection of light by the sun's gravitational field, from observations made at the total eclipse of may 29, 1919. Mem. R. Astron. Soc. **62**, A1 (1923)
2. C.W.F. Everitt et al., Gravity probe B: Final results of a space experiment to test general relativity. Phys. Rev. Lett. **106**, 221101 (2011). https://doi.org/10.1103/PhysRevLett.106.221101. arXiv:1105.3456
3. B.P. Abbott et al., Observation of Gravitational Waves from a Binary Black Hole Merger. Phys. Rev. Lett. **116**(6), 061102 (2016). https://doi.org/10.1103/PhysRevLett.116.061102. arXiv:1602.03837
4. D. Psaltis, Testing general relativity with the event horizon telescope. Gen. Rel. Grav. **51**(10), 137 (2019)
5. I.I. Shapiro, Fourth test of general relativity. Phys. Rev. Lett. **13**(26), 789 (1964)
6. J.H. Taylor, J.M. Weisberg, A new test of general relativity-gravitational radiation and the binary pulsar psr 1913+ 16. Astrophys. J. **253**, 908–920 (1982)
7. C.W. Misner, Classical and quantum dynamics of a closed universe, in *Relativity*. ed. by M. Carmeli, S.I. Fickler, L. Witten (Springer, US, Boston, MA, 1970), pp.55–79
8. H.-Y. Schive, T. Chiueh, T. Broadhurst, Cosmic Structure as the Quantum Interference of a Coherent Dark Wave. Nature Phys. **10**, 496–499 (2014). https://doi.org/10.1038/nphys2996. arXiv:1406.6586
9. G. Bertone, T. Tait, M. P., A new era in the search for dark matter. Nature **562**(7725), 51–56 (2018). https://doi.org/10.1038/s41586-018-0542-z. arXiv:1810.01668
10. S. Capozziello, V. Faraoni, Beyond Einstein gravity: A Survey of gravitational theories for cosmology and astrophysics, Vol. 170, Springer Science & Business Media (2010)
11. S. Capozziello, M. De Laurentis, Invariance principles and extended gravity: theory and probes, Nova Science Publishers, Inc., (2011)
12. S. Capozziello, M. De Laurentis, Extended theories of gravity. Phys. Rep. **509**(4–5), 167–321 (2011)
13. M. De Laurentis, I. De Martino, R. Lazkoz, Analysis of the Yukawa gravitational potential in $f(R)$ gravity II: relativistic periastron advance. Phys. Rev. D **97**(10), 104068 (2018). https://doi.org/10.1103/PhysRevD.97.104068. arXiv:1801.08136
14. C. Bambi, Black Holes: A Laboratory for Testing Strong Gravity, Springer Singapore. Singapore (2017). https://doi.org/10.1007/978-981-10-4524-0
15. X.-M. Deng, Geodesics and periodic orbits around quantum-corrected black holes. Phys. Dark Univ. **30**, 100629 (2020). https://doi.org/10.1016/j.dark.2020.100629
16. S. Yang, Y.-P. Zhang, T. Zhu, L. Zhao, Y.-X. Liu, Gravitational waveforms from periodic orbits around a quantum-corrected black hole. JCAP **01**, 091 (2025). https://doi.org/10.1088/1475-7516/2025/01/091. arXiv:2407.00283
17. K. Glampedakis, Extreme mass ratio inspirals: Lisa's unique probe of black hole gravity. Class. Quantum Gravity **22**(15), S605 (2005). https://doi.org/10.1088/0264-9381/22/15/004
18. S. Babak, H. Fang, J.R. Gair, K. Glampedakis, S.A. Hughes, "Kludge" gravitational waveforms for a test-body orbiting a Kerr black hole. Phys. Rev. D **75**, 024005 (2007) [Erratum: Phys.Rev.D 77, 04990 (2008)]. https://doi.org/10.1103/PhysRevD.75.024005, arXiv:gr-qc/0607007
19. O. Shabbir, M. Jamil, M. Azreg-Aïnou, Periodic orbits and their gravitational wave radiations around the schwarzschild-mog black hole. Physics of the Dark Universe **47**, 101816 (2025)
20. J. Levin, R. Grossman, Dynamics of black hole pairs. i. periodic tables. Phys. Rev. D **79**, 043016 (2009). https://doi.org/10.1103/PhysRevD.79.043016
21. R. Grossman, J. Levin, Dynamics of black hole pairs. ii. spherical orbits and the homoclinic limit of zoom-whirliness. Phys. Rev. D **79**, 043017 (2009). https://doi.org/10.1103/PhysRevD.79.043017
22. G.Z. Babar, A.Z. Babar, Y.-K. Lim, Periodic orbits around a spherically symmetric naked singularity. Physical Review D **96**(8), 084052 (2017)

23. L. Stella, M. Vietri, S. Morsink, Correlations in the qpo frequencies of low mass x-ray binaries and the relativistic precession model. Astrophys. J. Lett. **524**, L63–L66 (1999). https://doi.org/10.1086/312291. arXiv:astro-ph/9907346
24. M. van der Klis, Millisecond oscillations in x-ray binaries. Ann. Rev. Astron. Astrophys. **38**, 717–760 (2000). https://doi.org/10.1146/annurev.astro.38.1.717. arXiv:astro-ph/0001167
25. M. Rizwan, M. Jamil, K. Jusufi, Distinguishing a Kerr-like black hole and a naked singularity in perfect fluid dark matter via precession frequencies. Phys. Rev. D **99**(2), 024050 (2019). https://doi.org/10.1103/PhysRevD.99.024050
26. J. Rayimbaev, P. Tadjimuratov, A. Abdujabbarov, B. Ahmedov, M. Khudoyberdieva, Dynamics of Test Particles and Twin Peaks QPOs around Regular Black Holes in Modified Gravity. Galaxies **9**(4), 75 (2021). https://doi.org/10.3390/galaxies9040075
27. J. Rayimbaev, A. Abdujabbarov, H. Wen-Biao, Regular nonminimal magnetic black hole as a source of quasiperiodic oscillations. Phys. Rev. D **103**(10), 104070 (2021). https://doi.org/10.1103/PhysRevD.103.104070
28. J. Rayimbaev, A.H. Bokhari, B. Ahmedov, Quasiperiodic oscillations from noncommutative inspired black holes. Class. Quantum Gravity **39**(7), 075021 (2022). https://doi.org/10.1088/1361-6382/ac556a
29. J. Rayimbaev, A. Abdujabbarov, F. Abdulkhamidov, V. Khamidov, S. Djumanov, J. Toshov, S. Inoyatov, Quasiperiodic oscillation around charged black holes in Einstein-Maxwell-scalar theory. European Physical Journal C **82**(12), 1110 (2022). https://doi.org/10.1140/epjc/s10052-022-11080-8
30. J. Rayimbaev, B. Ahmedov, A.H. Bokhari, Constraints on charged black hole parameters using quasiperiodic oscillations data. International Journal of Modern Physics D **31**(11), 2240004–726 (2022). https://doi.org/10.1142/S0218271822400041
31. J. Rayimbaev, B. Majeed, M. Jamil, K. Jusufi, A. Wang, Quasiperiodic oscillations, quasinormal modes and shadows of Bardeen-Kiselev Black Holes. Physics of the Dark Universe **35**, 100930 (2022). arXiv:2202.11509, DOI: 10.1016/j.dark.2021.100930
32. J. Rayimbaev, F. Abdulxamidov, S. Tojiev, A. Abdujabbarov, F. Holmurodov, Test particles and quasiperiodic oscillations around gravitational aether black holes. Galaxies **11**(5) (2023). https://doi.org/10.3390/galaxies11050095, https://www.mdpi.com/2075-4434/11/5/95
33. J. Rayimbaev, R.C. Pantig, A. Övgün, A. Abdujabbarov, D. Demir, Quasiperiodic oscillations, weak field lensing and shadow cast around black holes in symmergent gravity. Ann. Phys. **454**, 169335 (2023). https://doi.org/10.1016/j.aop.2023.169335, https://www.sciencedirect.com/science/article/pii/S0003491623001215
34. J. Rayimbaev, K.F. Dialektopoulos, F. Sarikulov, A. Abdujabbarov, Quasiperiodic oscillations around hairy black holes in Horndeski gravity. European Physical Journal C **83**(7), 572 (2023). https://doi.org/10.1140/epjc/s10052-023-11769-4. arXiv:2307.03019
35. B. Toshmatov, O. Rahimov, B. Ahmedov, A. Ahmedov, Capture of Massless and Massive Particles by Parameterized Black Holes. Galaxies **9**(3), 65 (2021). https://doi.org/10.3390/galaxies9030065
36. B. Ahmedov, O. Rahimov, B. Toshmatov, Gravitational Capture Cross-Section of Particles by Schwarzschild-Tangherlini Black Holes. Universe **7**(8), 307 (2021). https://doi.org/10.3390/universe7080307
37. O. Rahimov, B. Toshmatov, Y. Vyblyi, A. Akhmedov, B. Abdulazizov, Charged particle dynamics in Reissner-Nordström-Tangherlini spacetime. Physics of the Dark Universe **44**, 101483 (2024). https://doi.org/10.1016/j.dark.2024.101483
38. B. Turimov, O. Rahimov, The Orbital and Epicyclic Frequencies in Axially Symmetric and Stationary Spacetime. Universe **8**(10), 507 (2022). https://doi.org/10.3390/universe8100507
39. B. Turimov, O. Rahimov, B. Ahmedov, Z. Stuchlík, K. Boymurodova, Dynamical motion of matter around a charged black hole. International Journal of Modern Physics D **30**(5), 2150037–407 (2021). https://doi.org/10.1142/S0218271821500371
40. B. Turimov, A. Mamadjanov, O. Rahimov, Hawking Radiation and Lifetime of Primordial Black Holes in Braneworld. Galaxies **11**(3), 70 (2023). https://doi.org/10.3390/galaxies11030070
41. O. Dönmez, Solving 1-d special relativistic hydrodynamics (srh) equations using different numerical methods and results from different test problems. Appl. Math. Comput. **181**(1), 256–270 (2006). https://doi.org/10.1016/j.amc.2006.01.031, https://www.sciencedirect.com/science/article/pii/S0096300306000956
42. O. Donmez, Perturbing the Stable Accretion Disk in Kerr and 4D Einstein-Gauss-Bonnet Gravities: Comprehensive Analysis of Instabilities and Dynamics. Res. Astron. Astrophys. **24**(8), 085001 (2024). https://doi.org/10.1088/1674-4527/ad5b9e. arXiv:2310.13847
43. O. Donmez, Proposing a physical mechanism to explain various observed sources of QPOs by simulating the dynamics of accretion disks around the black holes. European Physical Journal C **84**(5), 524 (2024). https://doi.org/10.1140/epjc/s10052-024-12876-6. arXiv:2311.08388
44. O. Donmez, The comparison of alternative spacetimes using the spherical accretion around the black hole. Mod. Phys. Lett. A **39**(16), 2450076–665 (2024). https://doi.org/10.1142/S0217732324500767. arXiv:2405.15467
45. F. Koyuncu, O. Dönmez, Numerical simulation of the disk dynamics around the black hole: Bondi Hoyle accretion. Mod. Phys. Lett. A **29**, 1450115 (2014). https://doi.org/10.1142/S0217732314501156
46. O. Donmez, Dynamical evolution of the shock cone around 4D Einstein-Gauss Bonnet rotating black hole. Phys. Lett. B **827**, 136997 (2022). https://doi.org/10.1016/j.physletb.2022.136997. arXiv:2103.03160
47. O. Donmez, F. Dogan, The Shock Cone Instabilities and Quasi-Periodic Oscillations around the Hartle-Thorne Black Hole. Universe **10**(4), 152 (2024). https://doi.org/10.3390/universe10040152
48. O. Donmez, From Low- to High-Frequency QPOs around the Non-Rotating Hairy Horndeski Black Hole: Microquasar GRS 1915+105, arXiv e-prints (2024). https://doi.org/10.48550/arXiv.2408.10102, arXiv:2408.10102
49. O. Donmez, F. Dogan, Estimating the possible QPOs of M87* from the parameters of a hairy Kerr black hole, arXiv e-prints (2024). https://doi.org/10.48550/arXiv.2407.01478, arXiv:2407.01478,
50. M. Kološ, M. Shahzadi, A. Tursunov, Charged particle dynamics in parabolic magnetosphere around Schwarzschild black hole. European Physical Journal C **83**(4), 323 (2023). https://doi.org/10.1140/epjc/s10052-023-11498-8. arXiv:2304.13603
51. S.E. Motta, T.M. Belloni, L. Stella, T. Muñoz-Darias, R. Fender, Precise mass and spin measurements for a stellar-mass black hole through X-ray timing: the case of GRO J1655–40. Mon. Not. R. Astron. Soc. **437**(3), 2554–2565 (2014). https://doi.org/10.1093/mnras/stt2068. arXiv:1309.3652
52. C. Bambi, Testing the nature of the black hole candidate in GRO J1655-40 with the relativistic precession model, arXiv e-prints (2013). https://doi.org/10.48550/arXiv.1312.2228, arXiv:1312.2228
53. C. Liu, H. Siew, T. Zhu, Q. Wu, Y. Zhao, H. Xu, Constraints on hairy Kerr black hole with quasi-periodic oscillations, arXiv preprint arXiv:2311.12423 (2023)

54. S. Motta, T. Belloni, L. Stella, G. Pappas, J. Casares, A. Muñoz-Darias, M. Torres, I. Yanes-Rizo, Black hole mass and spin measurements through the relativistic precession model: XTE j1859+226. MNRAS **517**(1), 1469–1475 (2022). https://doi.org/10.1093/mnras/stac2142. arXiv:2209.10376
55. S. Motta, T. Munoz-Darias, A. Sanna, R. Fender, T. Belloni, L. Stella, Black hole spin measurements through the relativistic precession model: XTE J1550–564. MNRAS Letters **439**, 65 (2014). https://doi.org/10.1093/mnrasl/slt181. arXiv:1312.3114
56. S. Capozziello, A. Stabile, A. Troisi, The Newtonian Limit of f(R) gravity. Phys. Rev. D **76**, 104019 (2007). https://doi.org/10.1103/PhysRevD.76.104019. arXiv:0708.0723
57. A. Cruz-Osorio, S. Gimeno-Soler, J.A. Font, M. De Laurentis, S. Mendoza, Magnetized discs and photon rings around yukawa-like black holes. Phys. Rev. D **103**, 124009 (2021). https://doi.org/10.1103/PhysRevD.103.124009
58. I. De Martino, M. De Laurentis, F. Atrio-Barandela, S. Capozziello, Constraining f(r) gravity with planck data on galaxy cluster profiles. Monthly Notices of the Royal Astronomical Society **442**(2), 921–928 (2014). https://doi.org/10.1093/mnras/stu903, arXiv:https://academic.oup.com/mnras/article-pdf/442/2/921/5729104/stu903.pdf
59. M.P. Hobson, G.P. Efstathiou, A.N. Lasenby, General Relativity: An Introduction for Physicists, (Cambridge University Press, 2006)
60. H. Goldstein, Classical Mechanics, (Pearson Education India, 2011)
61. B. Gao, X.-M. Deng, Bound orbits around Bardeen black holes. Ann. Phys. **418**, 168194 (2020)
62. T. Zahra, M. Jamil, M. Azreg-Aïnou, Spin precession frequencies of a test gyroscope around a naked singularity and quasi-periodic oscillations. Nucl. Phys. B **1017**, 116954 (2025). arXiv:2505.06443, DOI: 10.1016/j.nuclphysb.2025.116954
63. J. Levin, G. Perez-Giz, A periodic table for black hole orbits. Physical Review D **77**(10), 103005 (2008)
64. S. Babak, H. Fang, J.R. Gair, K. Glampedakis, S.A. Hughes, "kludge" gravitational waveforms for a test-body orbiting a Kerr black hole. Physical Review D **75**(2), 024005 (2007)
65. A. Maselli, N. Franchini, L. Gualtieri, T.P. Sotiriou, S. Barsanti, P. Pani, Detecting fundamental fields with LISA observations of gravitational waves from extreme mass-ratio inspirals. Nature Astronomy **6**(4), 464–470 (2022)
66. D. Liang, R. Xu, Z.-F. Mai, L. Shao, Probing vector hair of black holes with extreme-mass-ratio inspirals. Physical Review D **107**(4), 044053 (2023)
67. Z.-Y. Tu, T. Zhu, A. Wang, Periodic orbits and their gravitational wave radiations in a polymer black hole in loop quantum gravity. Physical Review D **108**(2), 024035 (2023)
68. S. Yang, Y.-P. Zhang, T. Zhu, L. Zhao, Y.-X. Liu, Gravitational waveforms from periodic orbits around a quantum-corrected black hole, arXiv preprint arXiv:2407.00283 (2024)
69. J. Rayimbaev, N. Juraeva, M. Khudoyberdiyeva, A. Abdujabbarov, M. Abdullaev, Quasiperiodic oscillations and dynamics of test particles around regular-kiselev black holes. Galaxies **11**(6), 1 (2023). https://doi.org/10.3390/galaxies11060113, https://www.mdpi.com/2075-4434/11/6/113
70. J. Rayimbaev, B. Majeed, M. Jamil, K. Jusufi, A. Wang, Quasiperiodic oscillations, quasinormal modes and shadows of bardeen–kiselev black holes. Physics of the Dark Universe **35**, 100930 (2022). https://doi.org/10.1016/j.dark.2021.100930, https://www.sciencedirect.com/science/article/pii/S2212686421001461
71. K. Jusufi, M. Azreg-Aïnou, M. Jamil, S.-W. Wei, Q. Wu, A. Wang, Quasinormal modes, quasiperiodic oscillations, and the shadow of rotating regular black holes in nonminimally coupled Einstein-Yang-Mills theory. Phys. Rev. D **103**(2), 024013 (2021). https://doi.org/10.1103/PhysRevD.103.024013. arXiv:2008.08450
72. A. Kotrlová, G. Török, E. Šramková, Z. Stuchlík, Supercritical accretion onto spinning compact objects and models of high-frequency quasi-periodic oscillations observed in Galactic microquasars. Astron. Astrophys. **572**, A79 (2014). https://doi.org/10.1051/0004-6361/201424407. arXiv:1410.6129
73. S. Luigi, V. Mario, M.M. Sharon, Correlations in the quasi-periodic oscillation frequencies of low-mass X-ray binaries and the relativistic precession model. Astrophys. J. Lett. **524**, L63–L66 (1999). https://api.semanticscholar.org/CorpusID:118088797
74. S. Kato, Frequency correlations of QPOs based on a disk oscillation model in warped disks. Publ. Astron. Soc. Jpn. **59**(2), 451 (2007). https://doi.org/10.1093/pasj/59.2.451. arXiv:arXiv:astro-ph/0701085
75. Z. Stuchlík, M. Kološ, Models of quasi-periodic oscillations related to mass and spin of the gro j1655–40 black hole. Astronomy & Astrophysics **586**, A130 (2016). https://doi.org/10.1051/0004-6361/201526095
76. D.R. Pasham, T.E. Strohmayer, R.F. Mushotzky, A 400-solar-mass black hole in the galaxy m82. Nature **513**(7516), 74–76 (2014). https://doi.org/10.1038/nature13710
77. Z. Stuchlík, M. Kološ, Mass of intermediate black hole in the source M82 X-1 restricted by models of twin high-frequency quasi-periodic oscillations. MNRAS **451**(3), 2575–2588 (2015). https://doi.org/10.1093/mnras/stv1120. arXiv:1603.07339
78. P. Casella, G. Ponti, A. Patruno, T. Belloni, G. Miniutti, L. Zampieri, Weighing the black holes in ultraluminous X-ray sources through timing. MNRAS **387**(4), 1707–1711 (2008). https://doi.org/10.1111/j.1365-2966.2008.13372.x. arXiv:0804.3378
79. G.C. Dewangan, L. Titarchuk, R.E. Griffiths, Black Hole Mass of the Ultraluminous X-Ray Source M82 X-1. Astrophys. J. **637**(1), L21–L24 (2006). https://doi.org/10.1086/499235. arXiv:astro-ph/0509646
80. P. Mucciarelli, P. Casella, T. Belloni, L. Zampieri, P. Ranalli, A variable Quasi-Periodic Oscillation in M82 X-1. Timing and spectral analysis of XMM-Newton and RossiXTE observations, MNRAS **365**(4), 1123–1130 (2006). https://doi.org/10.1111/j.1365-2966.2005.09754.x. arXiv:astro-ph/0509796
81. H. Feng, P. Kaaret, Identification of the X-ray Thermal Dominant State in an Ultraluminous X-ray Source in M82. The Astrophysical Journal Letters **712**(2), L169–L173 (2010). https://doi.org/10.1088/2041-8205/712/2/L169. arXiv:1003.0283
82. A. Patruno, S. Portegies Zwart, J. Dewi, C. Hopman, The ultraluminous X-ray source in M82: an intermediate-mass black hole with a giant companion. MNRAS **370**(1), L6–L9 (2006). https://doi.org/10.1111/j.1745-3933.2006.00176.x. arXiv:astro-ph/0602230
83. X.-L. Zhou, S.-N. Zhang, D.-X. Wang, L. Zhu, Calibrating the Correlation Between Black Hole Mass and X-ray Variability Amplitude: X-ray Only Black Hole Mass Estimates for Active Galactic Nuclei and Ultra-luminous X-ray Sources. Astrophys. J. **710**(1), 16–23 (2010). https://doi.org/10.1088/0004-637X/710/1/16. arXiv:0912.2636
84. J.F. Steiner, R.C. Reis, J.E. McClintock, R. Narayan, R.A. Remillard, J.A. Orosz, L. Gou, A.C. Fabian, M.A.P. Torres, The spin of the black hole microquasar XTE J1550–564 via the continuum-fitting and Fe-line methods. MNRAS **416**(2), 941–958 (2011). https://doi.org/10.1111/j.1365-2966.2011.19089.x. arXiv:1010.1013
85. T.E. Strohmayer, Discovery of a 450 HZ Quasi-periodic Oscillation from the Microquasar GRO J1655–40 with the Rossi X-Ray Timing Explorer. Astrophys. J. **552**, L49–L53 (2001). https://doi.org/10.1086/320258

86. J.M. Miller, A.C. Fabian, J. Kaastra, T. Kallman, A.L. King, D. Proga, J. Raymond, C.S. Reynolds, Powerful, Rotating Disk Winds from Stellar-mass Black Holes. Astrophys. J. **814**(2), 87 (2015). https://doi.org/10.1088/0004-637X/814/2/87. arXiv:1510.01177
87. A.M. Ghez, S. Salim, N.N. Weinberg, J.R. Lu, T. Do, J.K. Dunn, K. Matthews, M.R. Morris, S. Yelda, E.E. Becklin, T. Kremenek, M. Milosavljevic, J. Naiman, Measuring Distance and Properties of the Milky Way's Central Supermassive Black Hole with Stellar Orbits. Astrophys. J. **689**, 1044–1062 (2008). https://doi.org/10.1086/592738. arXiv:0808.2870
88. D. Foreman-Mackey, D.W. Hogg, D. Lang, J. Goodman, emcee: The MCMC Hammer. PASP **125**(925), 306 (2013). https://doi.org/10.1086/670067. arXiv:1202.3665
89. A. Zhadyranova, M. Koussour, S. Bekkhozhayev, V. Zhumabekova, J. Rayimbaev, Exploring late-time cosmic acceleration: A study of a linear f(t) cosmological model using observational data. Physics of the Dark Universe **45**, 101514 (2024). https://doi.org/10.1016/j.dark.2024.101514, https://www.sciencedirect.com/science/article/pii/S2212686424000967
90. C. Liu, H. Xu, H. Siew, T. Zhu, Q. Wu, Y. Zhao, Constraints on the rotating self-dual black hole with quasi-periodic oscillations, arXiv e-prints (2023). https://doi.org/10.48550/arXiv.2305.12323, arXiv:2305.12323
91. S. Jumaniyozov, M. Zahid, M. Alloqulov, I. Ibragimov, J. Rayimbaev, S. Murodov, Radiative properties and QPOs around charged black hole in Kalb-Ramond gravity. European Physical Journal C **85**(2), 126 (2025). https://doi.org/10.1140/epjc/s10052-025-13863-1
92. S. Jumaniyozov, S.U. Khan, J. Rayimbaev, A. Abdujabbarov, S. Urinbaev, S. Murodov, Circular motion and QPOs near black holes in Kalb-Ramond gravity. European Physical Journal C **84**(9), 964 (2024). https://doi.org/10.1140/epjc/s10052-024-13351-y
93. B. Rahmatov, M. Zahid, J. Rayimbaev, R. Rahim, S. Murodov, QPOs and circular orbits around black holes in Chaplygin-like cold dark matter. Chin. J. Phys. **92**, 143–165 (2024). https://doi.org/10.1016/j.cjph.2024.09.002
94. J. Rayimbaev, S. Murodov, A. Shermatov, A. Yusupov, QPOs from charged particles around magnetized black holes in braneworlds. European Physical Journal C **84**(10), 1114 (2024). https://doi.org/10.1140/epjc/s10052-024-13463-5
95. S. Murodov, J. Rayimbaev, B. Ahmedov, E. Karimbaev, Quasiperiodic Oscillations and Dynamics of Test Particles around Quasi- and Non-Schwarzschild Black Holes. Universe **9**(9), 391 (2023). https://doi.org/10.3390/universe9090391
96. J. Rayimbaev, N. Juraeva, M. Khudoyberdiyeva, A. Abdujabbarov, M. Abdullaev, Quasiperiodic Oscillations and Dynamics of Test Particles around Regular-Kiselev Black Holes. Galaxies **11**(6), 113 (2023). https://doi.org/10.3390/galaxies11060113
97. J. Rayimbaev, U. Eshimbetov, B. Majeed, A. Abdujabbarov, A. Abduvokhidov, B. Abdulazizov, A. Xalmirzayev, Test particles and quasiperiodic oscillations around Kiselev black hole with cloud of strings. Chin. Phys. C **48**(5), 055104 (2024). https://doi.org/10.1088/1674-1137/ad2060
98. A. Caliskan, G. Mustafa, T. Naseer, S.K. Maurya, E. Güdekli, S. Murodov, F. Atamurotov, Particle dynamics with trajectories and epicyclic oscillations around a piece-wise black hole immersed in dark matter. Journal of High Energy Astrophysics **44**, 99–115 (2024). https://doi.org/10.1016/j.jheap.2024.09.005
99. G. Mustafa, E. Demir, F. Javed, S.K. Maurya, E. Güdekli, S. Murodov, F. Atamurotov, Epicyclic oscillations and particle collision with trajectories around quantum corrected black holes. Physics of the Dark Universe **46**, 101708 (2024). https://doi.org/10.1016/j.dark.2024.101708
100. S. Mitra, J. Vrba, J. Rayimbaev, Z. Stuchlik, B. Ahmedov, Charged particles and quasiperiodic oscillations in Black-bounce-Reissner-Nordström geometry in braneworlds. Physics of the Dark Universe **46**, 101561 (2024). https://doi.org/10.1016/j.dark.2024.101561
101. J. Levin, Energy level diagrams for black hole orbits. Class. Quantum Gravity **26**(23), 235010 (2009)